5 ROCK MECHANICS

5.1 Analysis Plan for Structural Evaluation of WIPP...

Sandia National Laboratories
Waste Isolation Pilot Plant

Structural Evaluation of WIPP Disposal Room Raised to Clay Seam G

AP-093

Task number
1.3.5.4.4.1

Effective Date: _12/10/02_

		Original signed by	
Author:	Byoung Yoon Park (6821)	*Byoung Yoon Park*	*12/9/2002*
	Print	Signature	Date
Technical Review:	Tom W. Pfeifle (6822)	*Original signed by* *Tom W. Pfeifle*	*12/9/2002*
	Print	Signature	Date
Management Review:	Francis D. Hansen (6822)	*Original signed by* *F.D. Hansen*	*12/9/02*
	Print	Signature	Date
QA Review:	Mario Chavez (6820)	*Original signed by* *Mario Chavez*	*12/9/02*
	Print	Signature	Date

TABLE OF CONTENTS

LIST OF TABLES

LIST OF FIGURES

1 INTRODUCTION AND OBJECTIVES

This analysis plan is necessary to determine the structural response of waste-filled disposal rooms raised 2.43 meters above the present level. The analysis period is 10,000 years after waste emplacement. The calculations of the mechanical creep closure response of a disposal room with waste but without crushed salt backfill will be performed to allow three-dimensional porosity surfaces (Figure 1) to be constructed for WIPP performance assessment activities. On the basis of the calculations, an assessment will be made whether raising the repository to Clay Seam G has any significant impact on the conceptual models used in performance assessment.
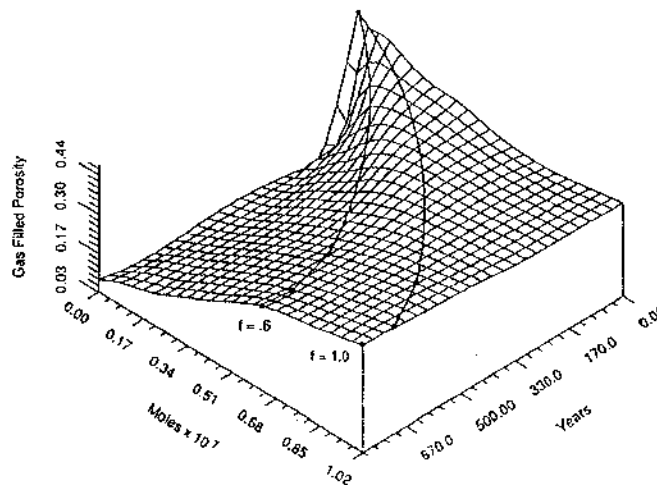
Figure 1: A typical porosity surface

The WIPP management and operating contractor, Westinghouse TRU Solutions (WTS), has asked permission of the EPA to raise the disposal room 2.43 m above the present level. This change means the roof of a disposal room would coincide with the Clay Seam G horizon and the floor would be separated from the underlying Marker Bed 139 by 3.81 m instead of 1.38 m (the existing separation in disposal panels 1 and 2). The structural implications of raising the repository horizon will be assessed using the calculations described in this Analysis Plan.

The change in repository horizon was recommended to ease ground control conditions. Fractures surrounding the existing horizon tend to coalesce in an arch, which mimics the shear stress trajectories. These patterns can be seen in the underground today where the roof has been taken down along the length of the East 140 drift. The roof rock of the original horizon tends to de-couple at Clay G, as exhibited by the shear fracture patterns. Underground operations personnel are currently obligated to provide roof support and maintenance that they believe would be unnecessary if the roof of the disposal rooms is

raised to Clay G. Because this change incorporates geometry in the WIPP underground that is different from the compliance baseline as modeled for the compliance application, it is necessary to evaluate the impact of this proposed mining change.

This analysis will be based on the "Final Disposal Room Structural Response Calculations, SAND97-0795" (Stone, C.M., 1997), which is the referenced baseline report for the CCA. Calculation procedures and data of SAND97-0795 will be used in this analysis and the results of this analysis will be compared with the results of SAND97-0795. Therefore, the initial calculations will replicate room pressure and porosity histories for various gas generation rates for a period of 10,000 years following excavation and waste emplacement.

2   APPROACH

2.1   Change the elevation of disposal rooms

Figure 2 shows the simplified stratigraphic model used for the disposal room analyses of SAND97-0795 (Butcher, 1997). This stratigraphic model will be changed as shown in Figure 2 to raise the disposal room by 2.43 m. The mesh for the FEM analysis will be changed as shown in Figure 3. The mesh, excluding the elements immediately adjacent to the room, is the same as the one made by Stone, C.M. (1997). The mesh will be changed as little as possible to minimize the margin of error resulting from the change. The new two-dimensional (2D) mesh will be made by modifying the FASTQ input file of Stone.
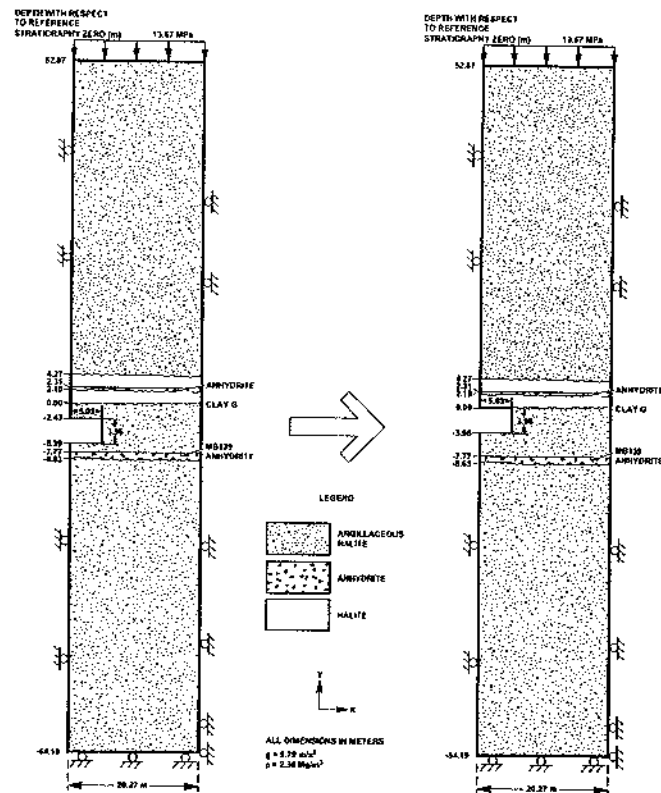
Figure 2: Simplified stratigraphic model used for the earlier disposal room analyses (left) and the new one (right).

original mesh   room elevation changed
2.43 m higher
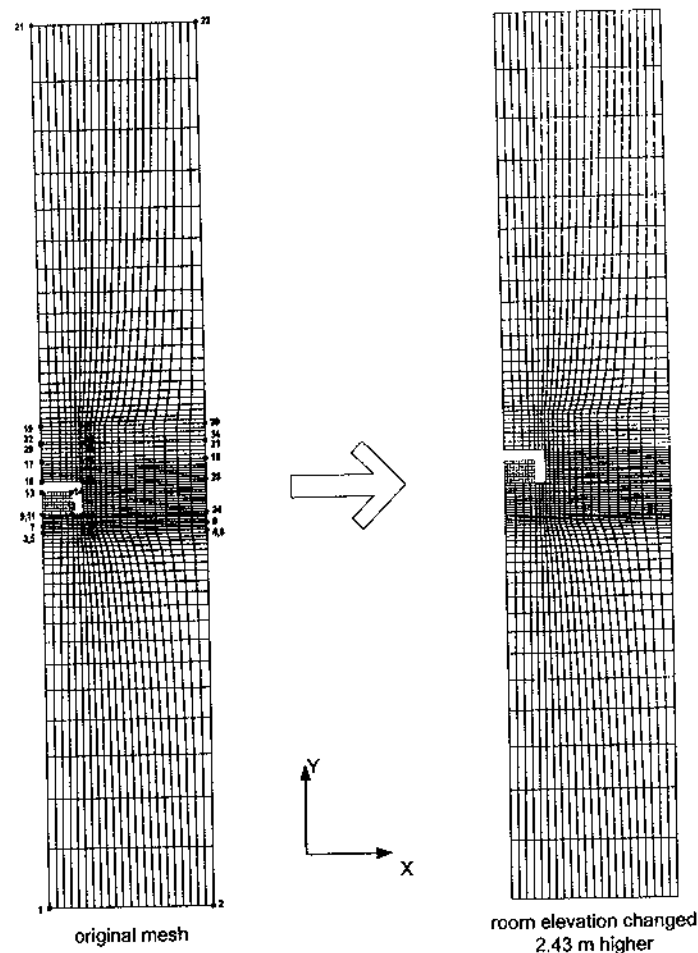
Figure 3: Mesh for FEM analyses

2.2 Solver

The quasistatic, large-deformation finite element code SANTOS (Stone, C.M., 1997), version 2.0.0 installed on the Sandia Cray J916 computer, was used for the earlier analysis. SANTOS is capable of representing 2D planar or axisymmetric solids. The solution strategy, used to obtain the equilibrium states, is based on a self-adaptive, dynamic-relaxation solution scheme incorporating proportional damping. The explicit nature of the code means that no stiffness matrix is formed or factorized which results in a reduction in the amount of computer storage necessary for execution. The element used in SANTOS is a uniform-strain, 4-node, quadrilateral element with an hourglass control scheme to minimize the effects of spurious deformation modes. Finite strain constitutive models for many common engineering materials were available within the code. A robust master-slave contact algorithm for modeling arbitrary sliding contact was implemented.

Recently, an executable SANTOS version 2.1.0 was installed on a Workstation with the Unix operating system. The source code of SANTOS was copied to the Workstation and compiled again. This SANTOS Workstation version will be used in this analysis.

The 2D "M-D Creep Model" (Munson, D.E. and Dawson, P.R., 1982) will be used for argillaceous halite or pure halite. The 2D "Soil n Foams Model" of SANTOS for anhydrite or waste packages also will be used.

2.3 Material data

The SANTOS data for each material will be identical to that used in Stone's analysis (Stone, C.M., 1997). The material constants corresponding to the clean and argillaceous salt, which will be used in the analyses, are given in Table 1 and Table 2.

Table 1: Clean and argillaceous salt elastic properties (Munson et al., 1989)

G MPa	E MPa	ν
12,400	31,000	0.25

Table 2: Salt creep properties (Munson et al., 1989)

Parameters (Units)	Clean Salt	Argillaceous Salt
A_1 (/sec)	8.386E22	1.407E23
Q_1 (cal/mole)	25,000	25,000
n_1	5.5	5.5
B_1 (/sec)	6.086E6	8.998E6
A_2 (/sec)	9.672E12	1.314E13
Q_2 (cal/mole)	10,000	10,000
n_2	5.0	5.0
B_2 (/sec)	3.034E-2	4.289E-2
σ_0 (MPa)	20.57	20.57
q	5,335	5,335
m	3.0	3.0
K_0	6.275E5	2.470E6
c (/T)	9.198E-3	9.198E-3
α_w	-17.37	-14.96
β_w	-7.738	-7.738
δ	0.58	0.58

Table 3 lists the pressure-volumetric strain data used for the waste drum model and the data are plotted in Figure 4. Note that the final point listed in the table is a linear extrapolation beyond the curve given in Butcher (1997). The final pressure (or mean stress) of 12 MPa corresponds to axial and radial stresses on a waste drum of 36 MPa and 0 MPa, respectively. The elastic material parameters and constants defining the yield surface are given in Table 4. The elastic properties and Drucker-Prager constants, C and a, for the anhydrite are given in Table 5. Clay Seams will be treated in a manner consistent with Stone (1997)

Table 3: Pressure-volumetric strain data used in the volumetric-plasticity model for the waste drums (Butcher, 1997)

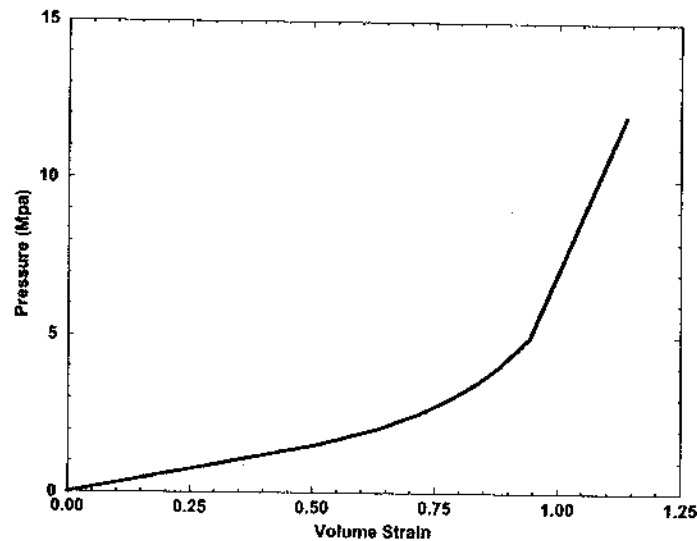| Pressure (MPa)	ln (ρ/ρ_0)
1.53	0.510
2.03	0.631
2.53	0.719
3.03	0.786
3.53	0.838
4.03	0.881
4.93	0.942
12.0	1.14

Figure 4: Curve of the pressure-bulk strain input to the volumetric plasticity model used to model the waste drums

Table 4: Material constants used with the volumetric plasticity model for the waste (Butcher, 1997)

Parameter	Value
G	333.0 MPa
K	222.0 MPa
a_0	1.0 MPa
a_1	3.0
a_2	0.

Table 5: Elastic and Drucker-Prager constants for anhydrite (Butcher, 1997)

Material	Young's Modulus (GPa)	Poisson's Ratio	C (MPa)	a
Anhydrite	75.1	0.35	1.35	0.45

2.4 Gas generation potential

The gas generation potential and gas production rate corresponding to the reference case are composed of gas from two sources: anoxic corrosion and microbial activity. Butcher(1997) reports that the estimated gas production potential from anoxic corrosion will be 1,050 *moles/drum* with a production rate of 1 *mole/drum/year*. The gas production potential from microbial activity is estimated to be 550 *moles/drum* with a production rate of 1 *mole/drum/year*. This means that microbial activity ceases at 550 years while anoxic corrosion will continue until 1,050 years after emplacement. The total amount of gas generated in a disposal room for the reference case was specified to be based on the 6,804 unprocessed waste drums per room. The total gas potential for the reference case is shown in Figure 5.

The gas pressure in the disposal room was computed from the ideal gas law based on the current free volume in the room. Specifically, the gas pressure, p_g, was computed with the following relationship:

$$p_g = f \cdot \frac{NRT}{V}$$

where N, R and T are the mass of gas in g-moles for the baseline case, the universal gas constant, and the absolute temperature in degrees Kelvin, respectively. For the current analyses, the absolute temperature is taken to be 300 °K. The variable is the current free volume of the room. During each iteration in the analysis, the current room volume is calculated based on the displaced positions of the nodes on the boundary of the room. The free room volume, V, is computed by subtracting the solid volume of the waste, 551.2 m³, from the current room volume. The gas generation variable, f, is a multiplier used in the analyses to scale the pressure by varying the amount of gas generation. A

value of $f=1$ corresponds to an analysis incorporating full gas generation, while a value of $f=0$ corresponds to an analysis incorporating no internal pressure increase due to gas generation. This portion of the analysis is identical to that implemented by Stone (1997).
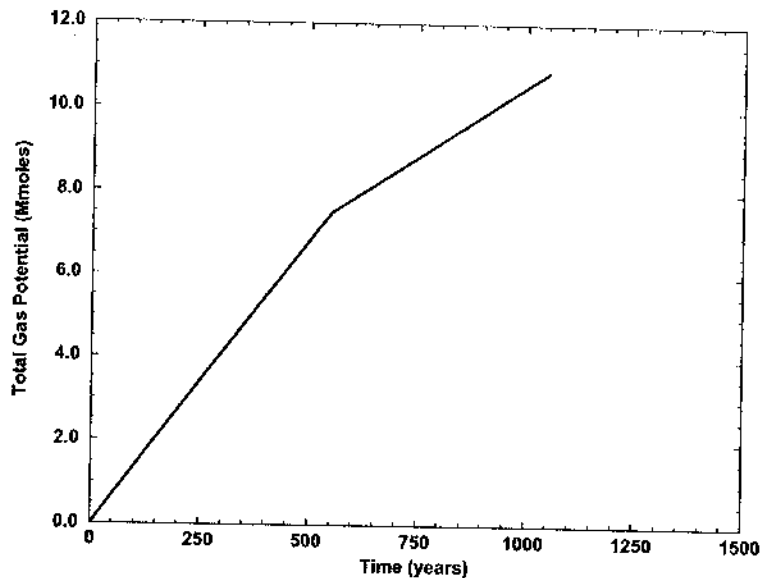
Figure 5: History of the reference gas generation potential used for the disposal room analyses, $f = 1.0$.

2.5 Subroutine

The previous analyses using SANTOS, version 2.0.0 installed on the Sandia Cray J916, were carried out to a simulation time of 10,000 years by Stone (1997). Thirteen cases of gas generation were investigated, these were for $f = 0.0$, 0.025, 0.05, 0.1, 0.2, 0.4, 0.5, 0.6, 0.8, 1.0, 1.2, 1.6, and 2.0. The gas generation parameter, f, was set in the user-supplied subroutine FPRES. The FPRES subroutine will be used unchanged in this analysis.

Stone (1997) used the user-supplied subroutine INITST to provide an initial stress state to SANTOS. In this analysis, the INITST subroutine will be used unchanged from Stone (1997).

3   SOFTWARE LIST

All applicable software and version numbers are listed in Table 6.

Table 6: Applicable software and version numbers

Code Name	Version
ALGEBRA2	1.15
APREPRO	1.60
BLOT	2.14S
SANTOS	2.1.0
FASTQ	2.1.0
GEN3D	1.16

4   TASKS

The following procedures will be performed to estimate whether raising the repository to Clay Seam G has any significant impact on the conceptual models used in performance assessment:

1. The effects of changing the FEM code on the calculated results will be qualified by comparing the results for the current horizon by SANTOS W/S version with the one by Stone (1997). That means, first the baseline results provided by Stone (1997) will be replicated.

2. The effects of raising the room 2.43 m will be calculated. The results for the disposal room raised 2.43 m will be compared with the baseline results replicated for the current horizon by SANTOS W/S version

3. Displacement data of the disposal room and wastes from SANTOS W/S version analyses will be converted into the porosity data by ALGEBRA. 3D porosity surface will be made of these porosity data with the gas generation potential and time.

4. The structural implication of raising the room 2.43 m will be evaluated by:

    o   Comparing MB139 to a failure criterion

    o   Examining stress conditions in the salt with respect to a damage function

Byoung Yoon Park will perform the analysis and be assisted in documentation by Tom W. Pfeifle and Francis D. Hansen. Mario Joseph Chavez will perform the QA procedures

assisted by Jose A. Archuleta. Quality insurance documentation, calculation runs, analysis and documentation are planned to be completed as expeditious as possible.

5   SPECIAL CONSIDERATIONS

No special considerations have been identified for this analysis.

6   APPLICABLE PROCEDURES

Analyses will be conducted in accordance with the quality assurance (QA) procedures listed below:

Training: Training will be performed in accordance with the requirements in NP 2–1, Qualification and Training.

Parameter Development and Database Management: Selection and documentation of parameter values will follow NP 9–2. The database is to be managed in accordance with relevant technical procedure.

Computer Codes: New or revised computer codes that will be used in the analyses will be qualified in accordance with NP 19–1. Codes will be run on the Compaq Tru64 UNIX V5.1A (Rev. 1885).

Analysis and Documentation: Documentation will meet the applicable requirements in NP 9–1.

Reviews: Reviews will be conducted and documented in accordance with NP 6–1 and NP 9–1, as appropriate.

7   REFERENCES

Butcher, B.M. 1997, *A Summary of the Sources of Input Parameter Values for the WIPP Final Porosity Surface Calculations*, SAND97-0796, Albuquerque, NM: Sandia National Laboratories.

Munson, D.E., and Dawson, P.R., 1982. *A Transient Creep Model for Salt during Stress Loading and Unloading*, SAND82-0962. Albuquerque, NM: Sandia National Laboratories.

Munson, D.E., Fossum, A.F., and Senseny, P.E., 1989, Advances in Resolution of Discrepancies between Predicted and Measured, In Situ Room Closures, SAND88-2948, Albuquerque, NM: Sandia National Laboratories.

Stone, C.M., 1997, *Final Disposal Room Structural Response Calculations,* SAND97-0795, Sandia National Laboratories, Albuquerque, NM.

5.2 DRZ Analyses[1]

D. M. Chapin, Jr. and F. D. Hansen
Sandia National Laboratories, MS 1395
4100 National Parks Hwy.
Carlsbad, NM 88220

Abstract

The disturbed rock zone (DRZ) surrounding underground openings in salt provides a path of increased permeability, which could bypass seals or closure systems installed in geologic radioactive waste repositories. Compliance application performance assessment calculations for salt repositories include characteristics and parameters of the DRZ that model brine influx into the disposal room and influence important evolutionary processes. Quantification of spatial and temporal characteristics plays a vital role in verification and validation of calculational and predictive methodologies. This paper presents petrophysical evidence of the structural state of the DRZ and excavation disturbed zone cores drilled from the Waste Isolation Pilot Plant salt repository and the German Asse Mine.

Introduction

This work is a continuation of ongoing studies of the disturbed rock zone (DRZ) and the excavation disturbed zone (EDZ) in halite, principally the microstructural analyses of WIPP and German salt cores. This work supports DRZ observational studies published previously (Bryan et al., 2001; Chapin and Hansen, 2002). Planning documents and the scientific notebooks controlling the petrographic structural analysis performed in this paper are Knowles (1999), Hansen and Bryan (2000), and laboratory notebooks WIPP-DRZ-Lab1, Lab2, and Lab3.

Microstructural features of fracture, free dislocation density and subgrain boundaries are analyzed for a variety of samples. The current work investigates salt cores procured from the WIPP repository, the German ALOHA II Project (Wieczorek and Zimmer, 1999), and from the Northern Test Drift B of the German Thermal and Structural Demonstration Experiment (TSDE) Test Field. The TSDE was conducted at the Asse Mine, near Braunschweig, Germany, by Gesellschaft fur Anlagen- und Reaktorsicherheit mbH (GRS). BAMBUS II (Backfill and Material Behavior in Underground Salt repositories) is the post-facto evaluation of the TSDE, and addresses the behavior of the EDZ, as well as backfill material within a geologic repository for heat-generating radioactive waste in rock salt. Its primary objectives are: (1) to increase the knowledge of important processes occurring in salt repository drifts, (2) to strengthen the scientific knowledge required for repository design and performance assessment, and (3) to help add to our knowledge of the geometry of the DRZ/EDZ and to delineate damage within this zone.

---

[1] This work is covered by WBS #1.3.5.4.4.1

Microstructural analyses entail: (1) petrographic fracture mapping; the creation of thick sections to investigate fracture densities, fracture apertures, fracture angles and the spatial distribution of fractures; (2) scanning electron microscopy (SEM) - geostatistical image analyses of dislocation pits observed on the surfaces of etched cleavage chips; (3) SEM analyses of subgrains and subgrain boundaries observed from etched cleavage chips extracted from disaggregated core samples. Free dislocation densities have been used as a correlative tool to support evidence of deformation processes, where a higher defect density correlates with higher strain magnitudes. Other substructural features, such as subgrain dimensions, decrease with increasing stress in both naturally and experimentally-deformed rock salts (Carter et al., 1982).

Core Samples

This observational study focuses on microstructural analyses of seven salt cores: (1) WIPP Core QGU14 (6.07 m), (2) WIPP Core QGU36 (7.33 m), (3) WIPP Core QGU39 (2.25 m), (4) Asse Mine Core DJ-V (6.97 m), (5) Asse Mine Core HD-V (6.83 m), (6) TSDE Core VVS-A-Mi4 (0.72 m), and (7) TSDE Core VVS-D1-Mi4 (0.77 m). The dimensions in parentheses indicate the lengths of the cores referenced from the opening or drift face in which the cores were recovered. The geology of WIPP QGU14 and QGU36 are similar; both are composed of elongate, coarse, clear halite and minor amounts of anhydrite. The first 2.5 m of WIPP QGU39 transitions between finer opaque halite to coarse, clear halite. Clay concentrations frequently appear along this opaque-clear boundary. All WIPP core was obtained by dry drilling (horizontally) through the inside rib of the 4-m high repository drift at a depth of 655 m. WIPP Core QGU14 was drilled normal to the rib at mid-height, whereas cores QGU36 and QGU39 were recovered from boreholes drilled into the corner of the Q-Room access drift (Figure 1). These cores, with an approximate coring axis angle of 45°–50° to the inside rib face (see Powers et al., 2001), extend through the DRZ and into the intact Salado Formation. Holcomb and Hardy (2001) have used ultrasonic wave velocities to delineate the DRZ in the WIPP, as a function of depth from the drift wall.

The two ALOHA II cores (DJ-V and HD-V) were drilled from the inside of the lined and unlined drifts of the 80-year-old Asse research mine, at a depth of 700 m, and were provided by K. Wieczorek. T. Rothfuchs from GRS provided the two TSDE cores for the purpose of performing the same petrographic microstructural analyses. Both TSDE cores were extracted from the Asse Mine's Northern Drift B, at the 800-m level (Figures 2 and 3), as part of the BAMBUS II collaborative work.
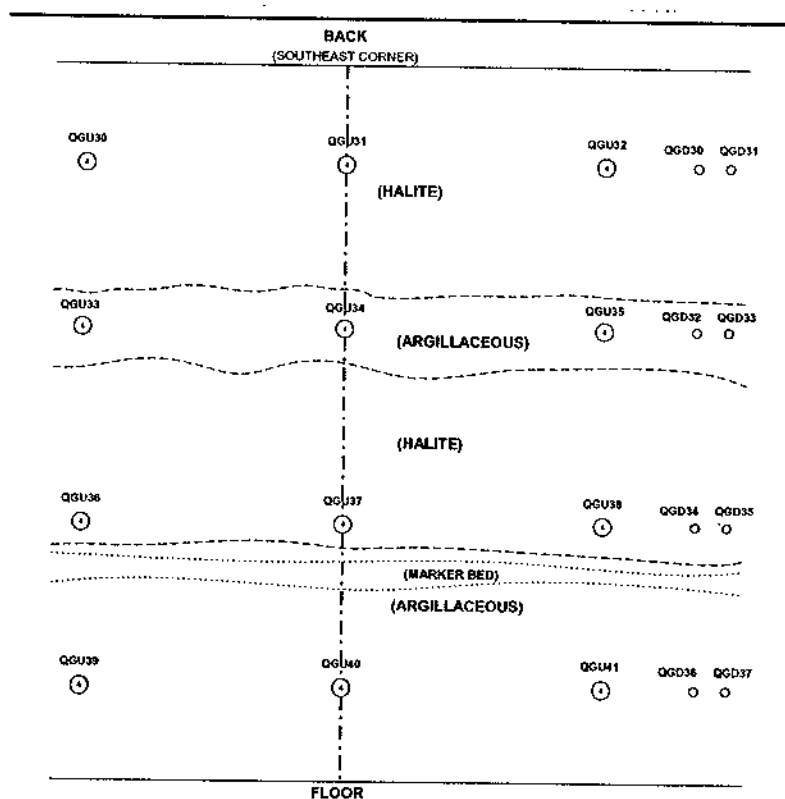
Figure 1. Layout of holes found in the Q-Room alcove; SE corner boreholes. WIPP coresQGU36 and QGU39 were recovered from the area shown in the lower left region. The 12 large holes, including hole QGU39, are used for sonic velocity measurements. The eight small holes were drilled for hydrologic analyses.

Methods

PETROGRAPHIC FRACTURE MAPPING

All core samples were halved lengthwise. Subsequently, one half was halved again to produce a one-quarter-core billet from which thick sections (approximately 1-mm-thick) could be fabricated. A diamond-impregnated wire-line saw was employed to cut the core and the billets to the appropriate geometry. Quartered billets were subsequently impregnated with fluorescent dyed Epo-thin epoxy, ground flat, mounted on 5-×-15-cm glass plates, then cut and polished as thick sections. Measurements of the fracture distributions, fracture apertures, and fracture spacing (distance from the inside rib face or wall) were taken across the centerline of each thick section (parallel to the core axis), which would intersect fractures oriented parallel to the drift axis and cross-cutting the core hole. In addition, fracture angles (the angle each fracture makes with respect to the core axis) were measured for WIPP cores QGU36 and QGU39.
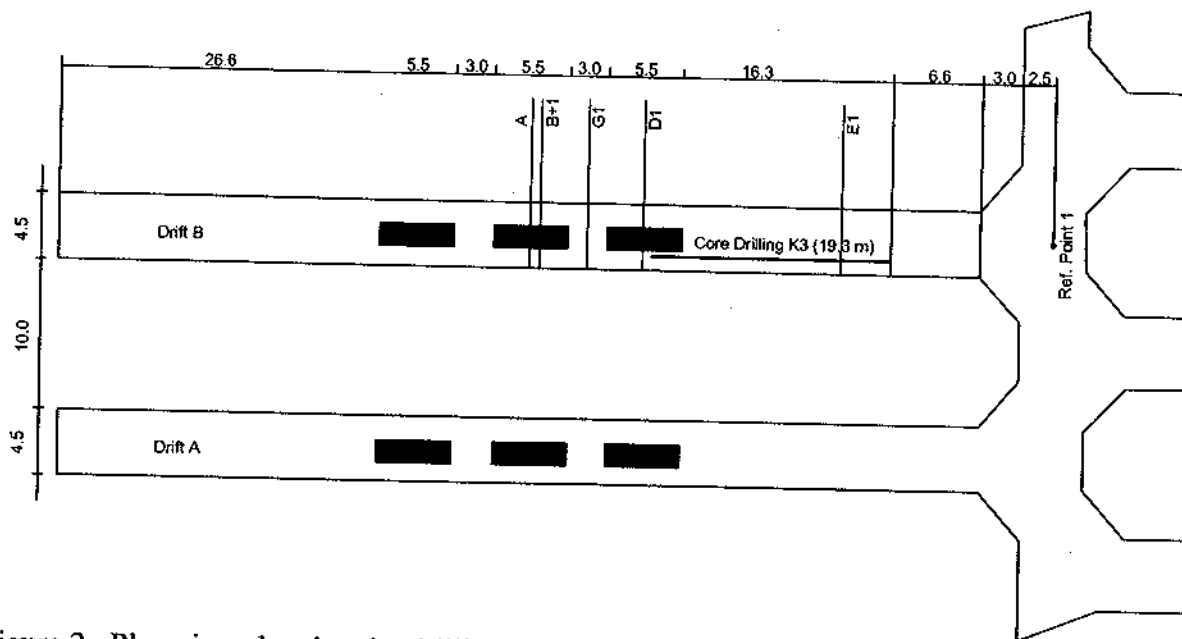
Figure 2. Plan view showing the drilling positions of EDZ sampling holes and surrounding host rock in the Northern Drift B of the TSDE Test Field. This investigation focuses, in part, on cores VVS-A-Mi4 and VVS-D1-Mi4 drilled from the Northern Drift B at a depth of 800 m.
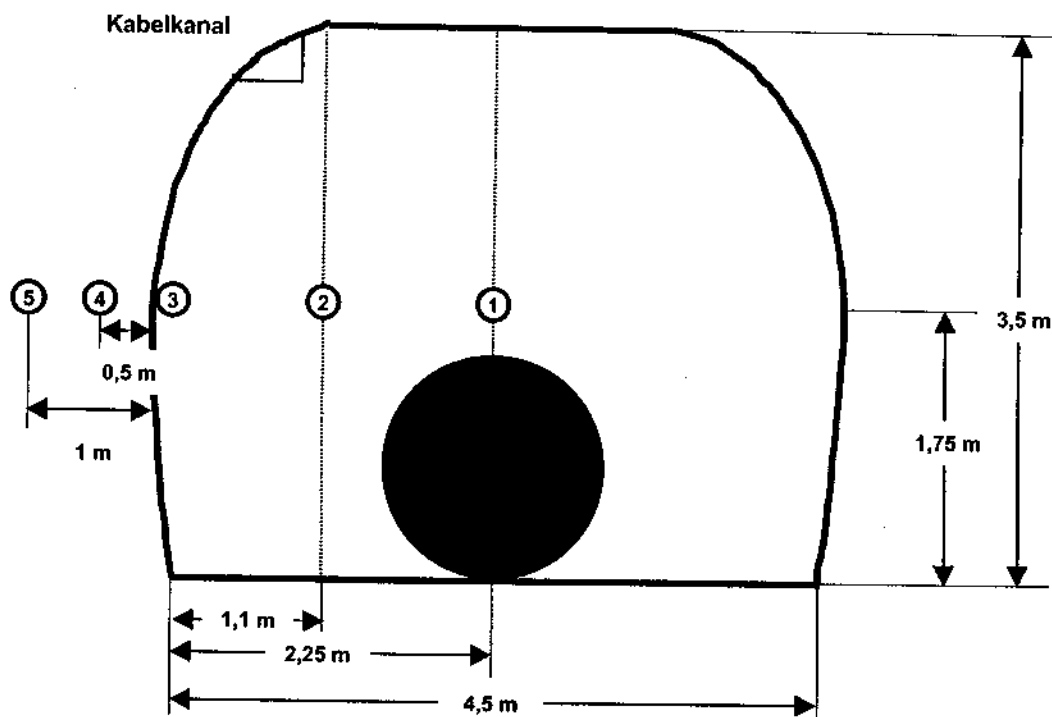
Figure 3. Northern drift cross-section showing the recovery locations of cores VVS-A-Mi4 and VVS-D1-Mi4. Cores VVS-A-Mi4 and VVS-D1-Mi4 were recovered from positions between locations 4 and 5 at horizontal distances of 0.83 m and 0.90 m, respectively.

DISLOCATION DENSITY

Dislocation density was determined using etch-pit techniques. Core samples were disaggregated whereupon individual crystal grains were cleaved. Cleavage chips were then etched in a saturated solution of $PbCl_2$ in methanol for 3 s and immediately rinsed in butanol to arrest the etch process. Free dislocation emergent sites preferentially etch owing to the strain energy in the salt crystal's distorted lattice. After etching, the cleavage chips were mounted on petrographic slides and sputter-coated using a Au-Pd target. Etch pits were subsequently imaged using a JEOL SEM and dislocation densities were determined using Image-Pro, a geostatistical, digital image processing software package.

SUBGRAIN ANALYSES

Etched cleavage chips (see Dislocation Densities above) were employed for this analysis. Subgrains were imaged using a JEOL SEM and then printed on paper. Subgrains were subsequently outlined in ink and then measured by hand to determine the total and mean structural sizes. Sizes were determined by averaging the lengths of the major and minor axes of each subgrain.

Results

FRACTURE ANALYSES

Results of the fracture analyses of the WIPP, ALOHA II and TSDE salt cores are presented in Table 1 and in Figures 4–9. Of the seven cores studied, three cores were analyzed throughout their complete length at a shallow distance into the rib: (1) WIPP Core QGU39 (2.25 m), (2) TSDE Core VVS-A-Mi4 (0.72 m), and (3) TSDE Core VVS-D1-Mi4 (0.77 m). WIPP Core QGU39 recorded the widest mean fracture apertures of the three, as well as the highest fracture density (Table 1). Observed mean fracture apertures in the TSDE cores are approximately half the width of those measured in QGU39, while their fracture density is approximately 75% that of QGU39.

The four remaining cores, WIPP Cores QGU14 (6.07 m) and QGU36 (7.33 m), as well as the ALOHA II Cores DJ-V (6.97 m) and HD-V (6.83 m) were analyzed differently. The complete first meter of each core was examined, and then subsequent fracture analyses were performed at 1-m intervals until the core length was exhausted. The WIPP cores have the higher mean fracture apertures (150–400% higher than the ALOHA II cores), whereas the ALOHA II cores have much higher fracture densities (200–400% higher than the WIPP cores; Table 1). Fracture porosity was measured from both the WIPP and ALOHA II cores (measured along the central transect through each of the polished thick sections). In the WIPP cores, the fracture porosity is largest proximal to the rib (QGU14 mean = 2.1% and QGU36 mean = 1.5% at a depth $\leq$ 2 m) and decreases consistently with increasing depth (QGU14 mean = 0.6% and QGU36 mean = 0.2% at a depth $\geq$ 2 m). The ALOHA II cores also exhibit higher porosity values closer
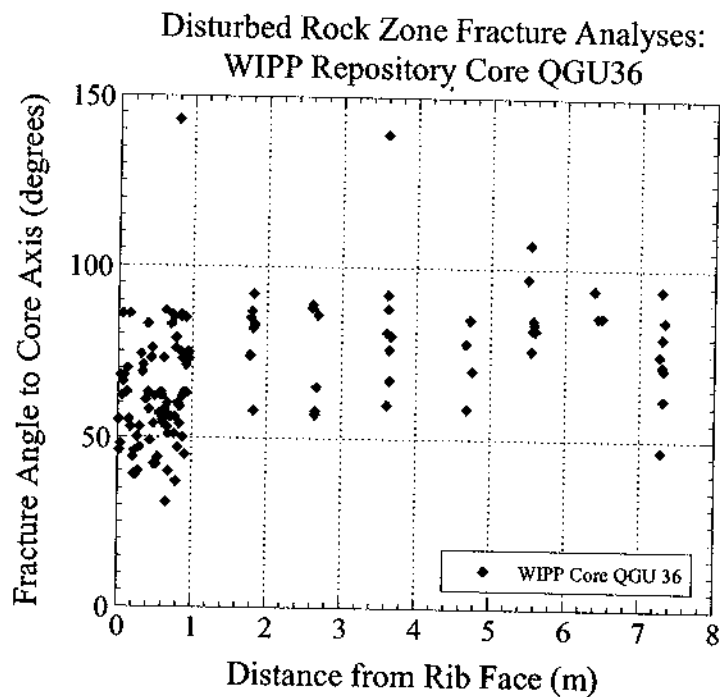
Figure 6. Plot showing the distribution of fracture angles observed in WIPP Core QGU36.
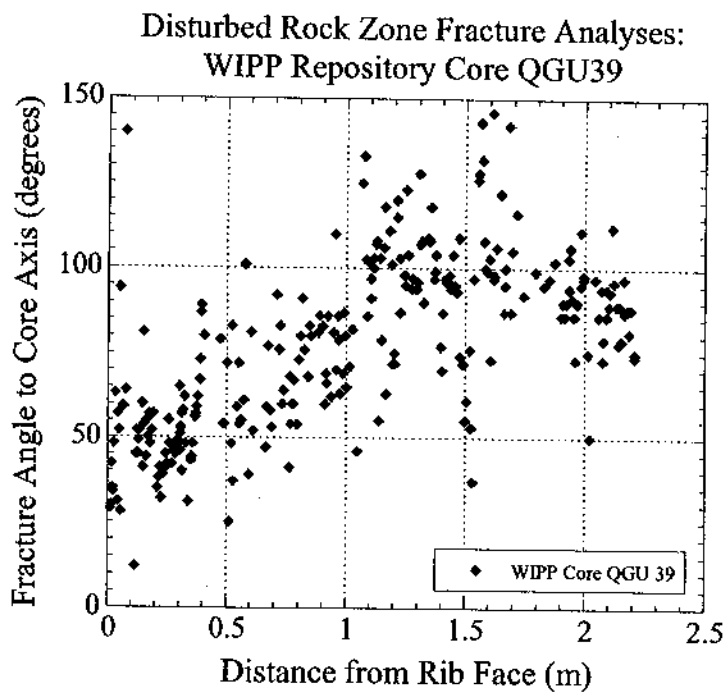

Figure 7. Plot showing the distribution of fracture angles in the first 2.25 m of WIPP Core QGU39.

A comparison of the fracture distributions and fracture apertures between ALOHA II Cores DJ-V and HD-V is presented in Figure 8. Except for a few wide fractures measured proximal to the rib wall in core DJ-V, there does not appear to be a large disparity between fracture density and fracture aperture as a function of depth between either the ALOHA II lined (DJ-V) and unlined (HD-V) drift samples.

EDZ Fracture Analyses: ALOHA II Cores
DJ-V (lined drift) and HD-V (unlined drift)
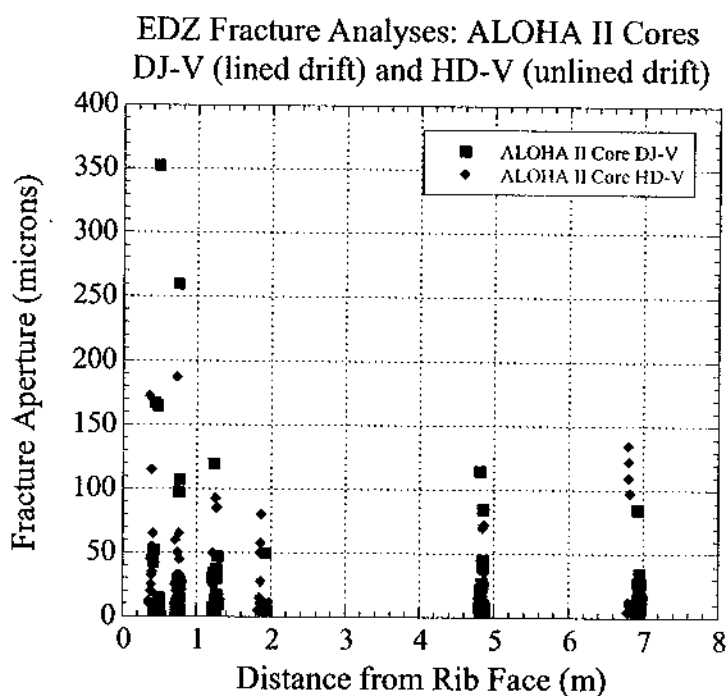
Figure 8. Plot showing the distribution of fractures and fracture apertures observed in the Asse Mine's ALOHA II Cores DJ-V (lined drift) and the HD-V (unlined drift).

Fracture distributions and fracture apertures for both TSDE cores appear to be quite similar along the complete lengths measured (Figure 9). The highest density of fractures in VVS-A-Mi4 and VVS-D1-Mi4 occurs in the first 0.5 m of each core, and except for a few outlier measurements, the apertures are wider proximal to the rib faces. TSDE fractures closest to the free surface are still much thinner compared to the WIPP and ALOHA II ambient cores.

Figure 9. Plot showing the distribution of fractures and fracture apertures observed in the first meter of cores VVS-A-Mi4 and VVS-D1-Mi4, Northern Test Drift B, TSDE Test Field, Germany.

A comparison of all seven cores is presented in Figure 10. The highest density of fractures is observed closest to the rib walls, at an approximate distance ≤ 2 m. Fracture apertures at a depth of 2 m or greater are predominantly ≤ 100 μm wide.
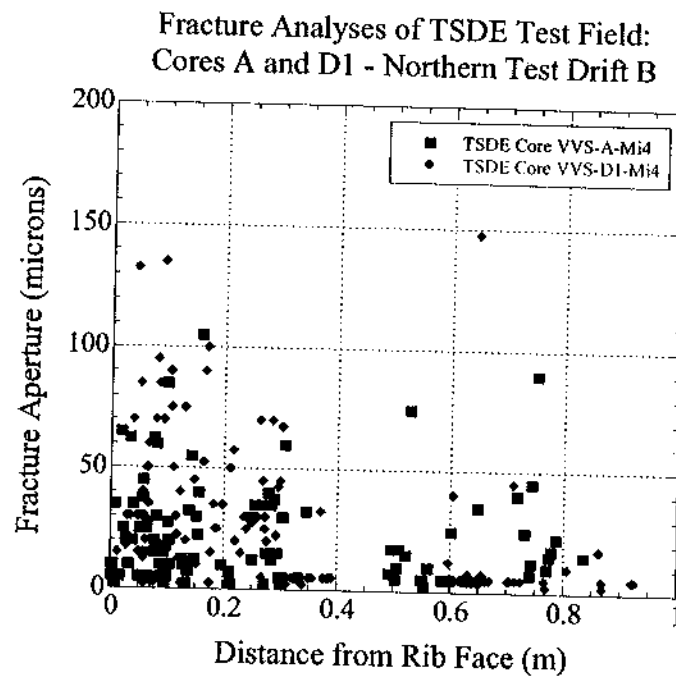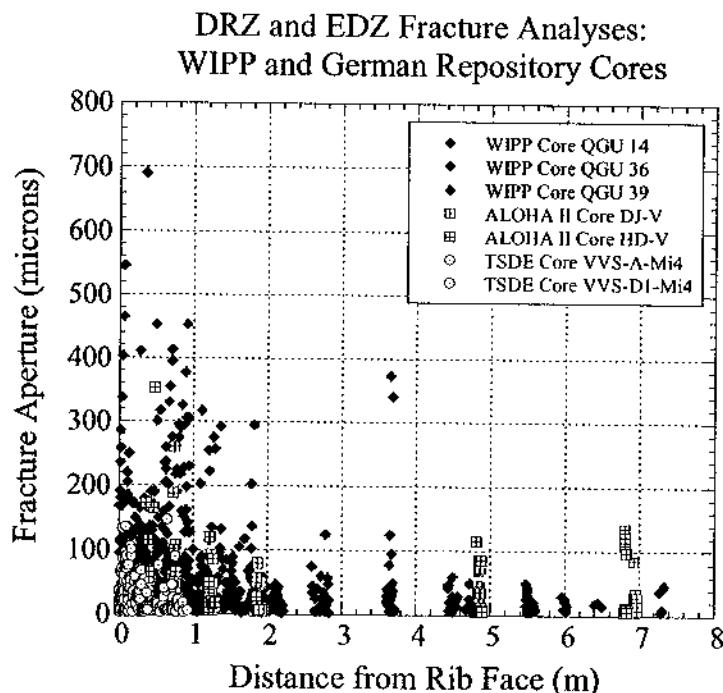

Figure 10. Plot showing the distribution of fractures and fracture apertures in core drilled from the WIPP, Asse Mine's ALOHA II drifts and the TSDE Test Field. Fracture distributions and apertures are plotted as a function of distance from the inside of the repository rib wall or face.

FREE DISLOCATION DENSITY

Photomicrographs of typical free dislocation etch-pits, as well as plots describing the free dislocation density distributions are presented as follows: (1) WIPP Core QGU14 (Figures 11-12), (2) the ALOHA II Cores DJ-V and HD-V (Figures 13-14), and (3) the TSDE Cores VVS-A-Mi4 and VVS-D1-Mi4 (Figures 15-16). Mean dislocation densities observed in core QGU14 are the highest of all the cores analyzed and are highest near the free surface, within the first 2 m. At a depth greater than 2 m, dislocation densities appear to decrease below the overall mean of 8×10^7 dislocations·cm^{-2} (Figure 12). Results comparing both ALOHA II cores are relatively similar (Figure 14), as the dislocation densities appear to level off to a background density of 7×10^7 dislocations·cm^{-2}, after an initially high-density spike inside the first 1.5 m. Free dislocation density of WIPP salt and ALOHA II salt has relatively the same magnitude and distribution. By comparison, both TSDE cores have significantly lower measured mean dislocation density (2.5×10^7 cm^{-2}) compared to the QGU14 and the ALOHA II cores. Density measurements from both TSDE samples are relatively uniform (Figure 16), in contrast to density increases near the rib found in the WIPP and ALOHA II salts.
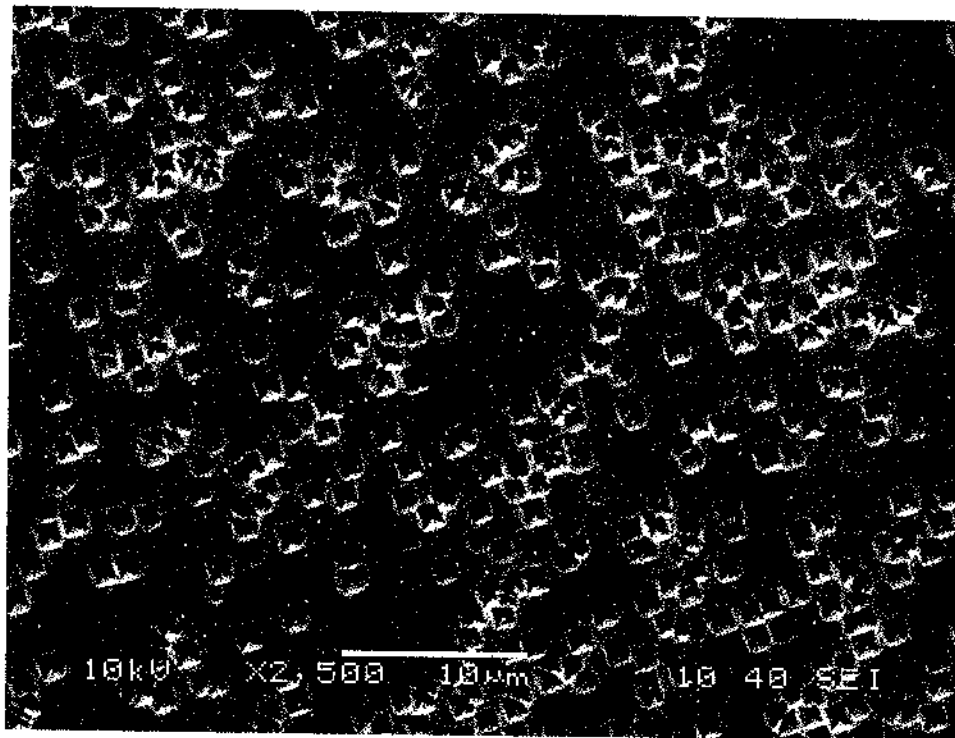
Figure 11. SEM image showing the distribution of free dislocation densities in cleavage chip QGU14-49.1, extracted from WIPP core QGU14-49 at a depth of approximately 6 m downhole (magnification: 2500X).

Figure 12. Plot showing the distribution of free dislocation densities measured from etched cleavage chips extracted from WIPP Core QGU14 (mean $= 8 \times 10^7$ dislocations·cm^{-2}).

(a)
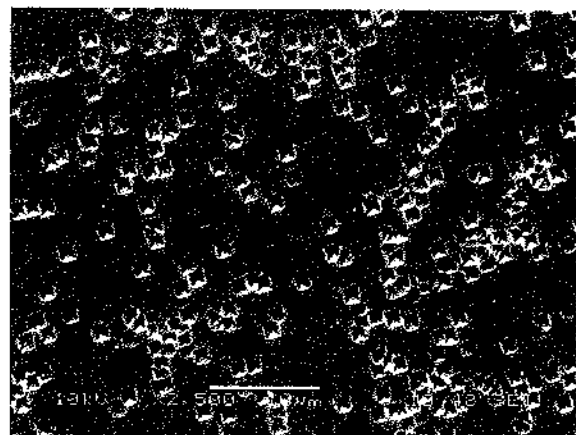
(b)

Figure 13. SEM images showing the distribution of free dislocation densities in cleavage chips: (a) DJ-V1.3, extracted from core ALOHA II DJ-V at a depth of approximately 0.5 m downhole (magnification: 2500X), and (b) HD-V6.3, extracted from the ALOHA II core HD-V at a depth of approximately 6.8 m downhole (magnification: 2500X).

Dislocation Densities: ALOHA II Core
DJ-V (lined drift) and HD-V (unlined drift)
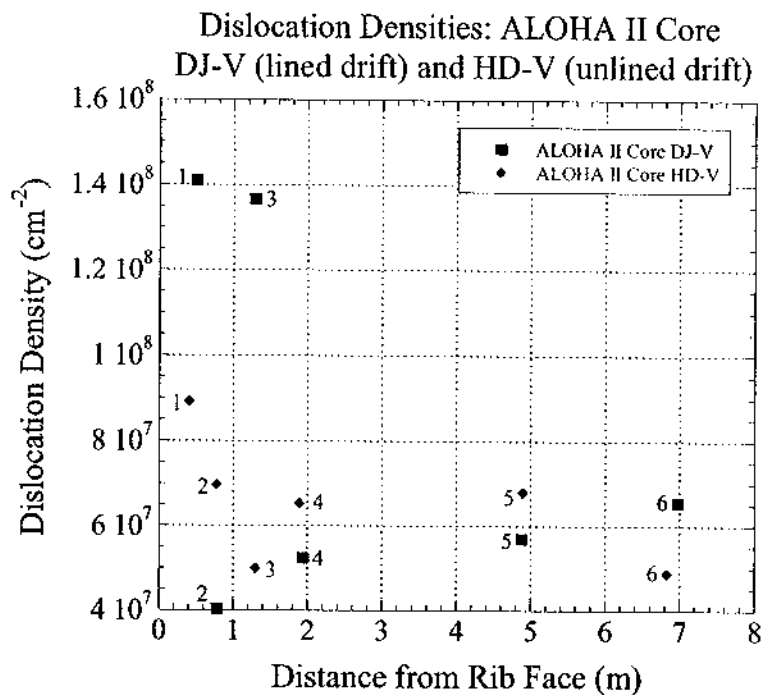
Figure 14. Plot showing the distribution of free dislocation densities measured from etched cleavage chips extracted from the ALOHA II Cores DJ-V (lined drift) and HD-V (unlined drift), Asse Mine, Germany (mean = 7×10^7 dislocations·cm^{-2}).
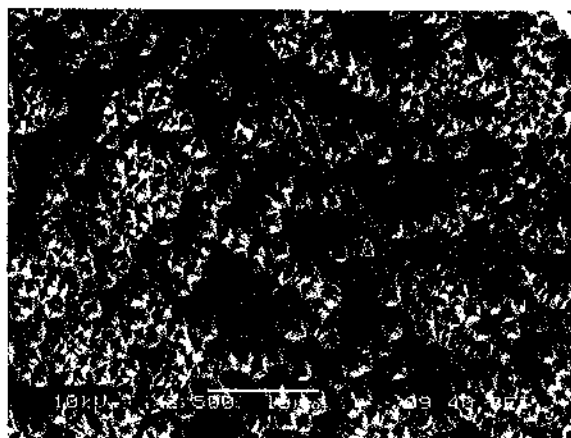
(a)
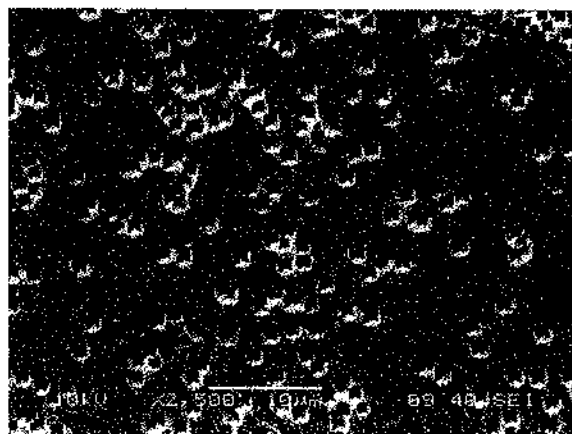
(b)
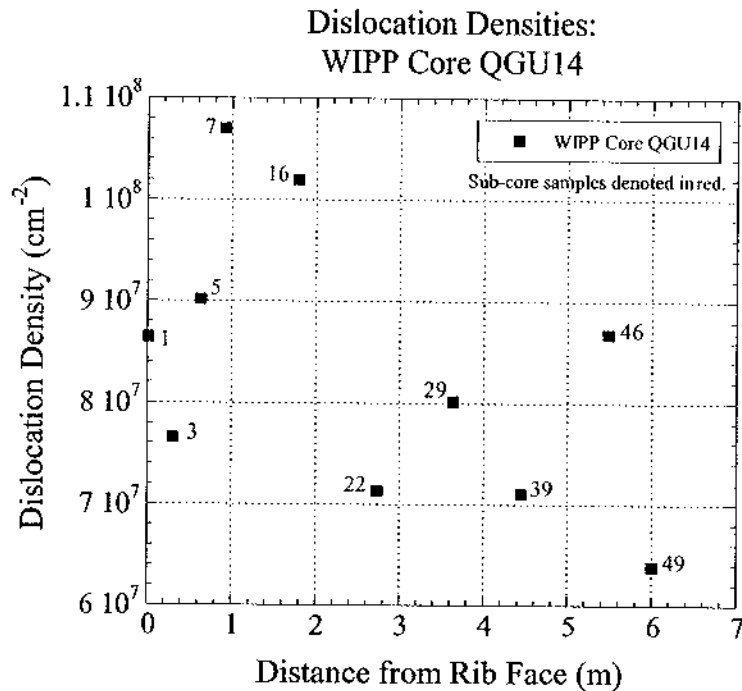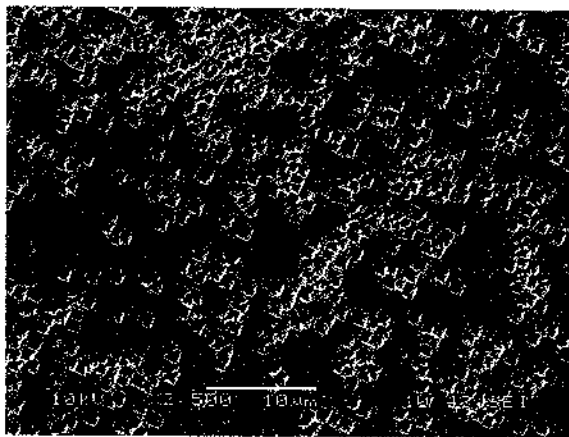
Figure 15. SEM images showing the distribution of free dislocation densities in etched cleavage chips: (a) TSDE A2.5, extracted from core VVS-A-Mi4, at a depth of approximately 0.3 m downhole (magnification: 2500X), and (b) TSDE D1.4.5, extracted from core VVS-D1-Mi4 at a depth of 0.85 m downhole, Northern Test Drift B (magnification: 2500X).
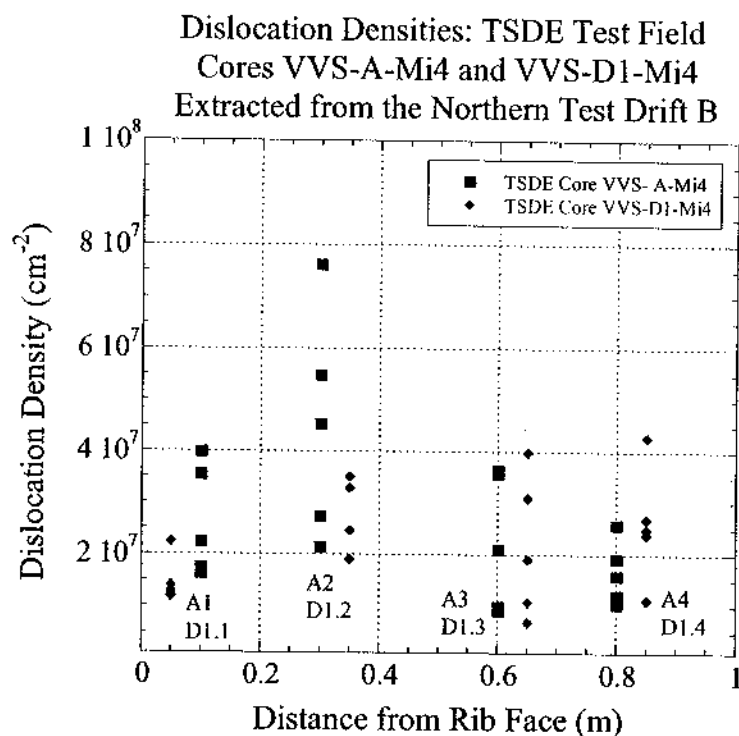
Figure 16. Plot showing the distribution of free dislocation densities measured from cleaved and etched chips extracted from the first meter of cores VVS-A-Mi4 and VVS-D1-Mi4, N. Test Drift B, TSDE Test Field, Germany (mean = 2.5 × 10^7 dislocations· cm^{-2}).

SUBGRAIN ANALYSES

Additional petrofabric analysis was performed on the TSDE cores, as they experienced significant strain in an elevated temperature condition. Therefore, the substructures found in the cores could substantiate the deformation mechanisms. One obvious substructural feature in natural and experimentally-deformed salt is subgrain size. As shown by Carter et al. (1982), the size of subgrains in salt is inversely proportional to the steady-state stress. A total of 2027 subgrains were measured in the first meter of both TSDE cores and an identical mean subgrain size was determined (57 μm in core A and 60 μm in core D1; Table 2, Figure 17). This subgrain size is relatively small, and thus represents a steady-state stress higher than experienced by other natural salts (as might be expected in this experimental configuration). A subgrain size of 60 μm correlates to a steady-state stress of approximately 3 MPa, according to a calibration plotted by Carter et al. (1982).

Table 2. Subgrain Analyses of TSDE Cores VVS-A-Mi4 and VVS-D1-Mi4.

Sample Analyzed	Distance (m)	Subgrain Density (cm^{-2})	Mean Sub-grain Size (μm)	SD (μm)	Minimum (μm)	Maximum (μm)
VVS-A1	0.1	206	64	35	5	175
VVS-A2	0.3	167	72	39	13	180
VVS-A3	0.6	274	51	33	8	180
VVS-A4	0.8	338	51	28	5	153
VVS-A1-4	0.83	985	57	34	5	180
VVS-D1-1	0.05	273	55	29	8	155
VVS-D1-2	0.35	229	60	34	5	175
VVS-D1-3	0.65	214	65	37	10	215
VVS-D1-4	0.85	326	49	29	5	158
VVS-D1-1-4	0.9	1042	60	33	5	215
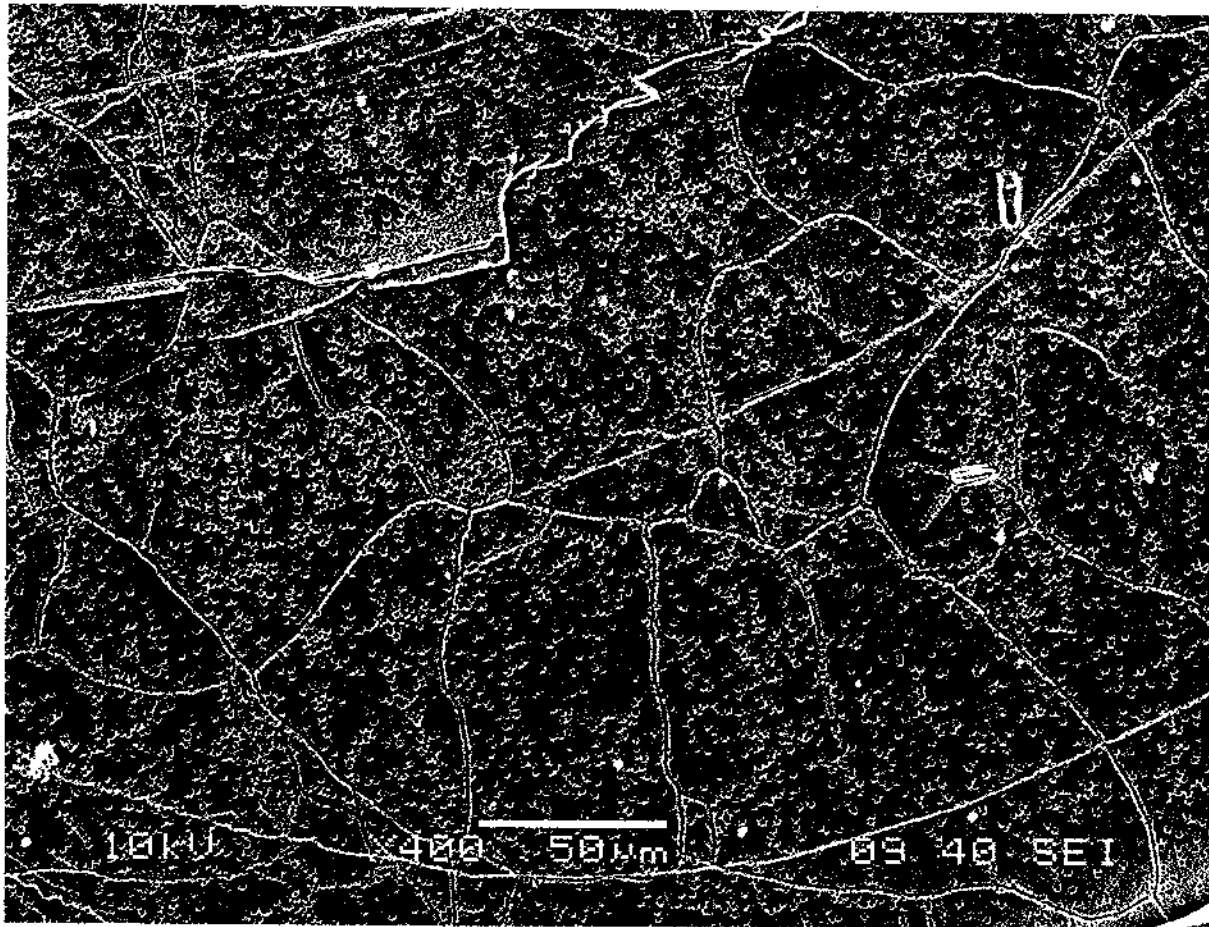
Figure 17. SEM photomicrograph showing subgrain boundaries and free dislocations imaged from cleavage chip TSDE A3.3, extracted from core TSDE VVS-A-Mi4 approximately 0.6 m downhole, Northern Test Drift B (magnification: 400X).

Glide bands are observed in TSDE samples containing the highest density of dislocations, typically greater than 4×10^7 cm^{-2} (Figure 18). Overall mean measurements of: (1) subgrain densities, (2) mean subgrain sizes and the standard deviation between sizes, and (3) the minimum and maximum subgrain sizes are essentially identical for both cores (see VVS-A1-4 and VVS-D1-1-4 of Table 2), although individual core measurements as a function of downhole depth are quite variable (Figure 19).
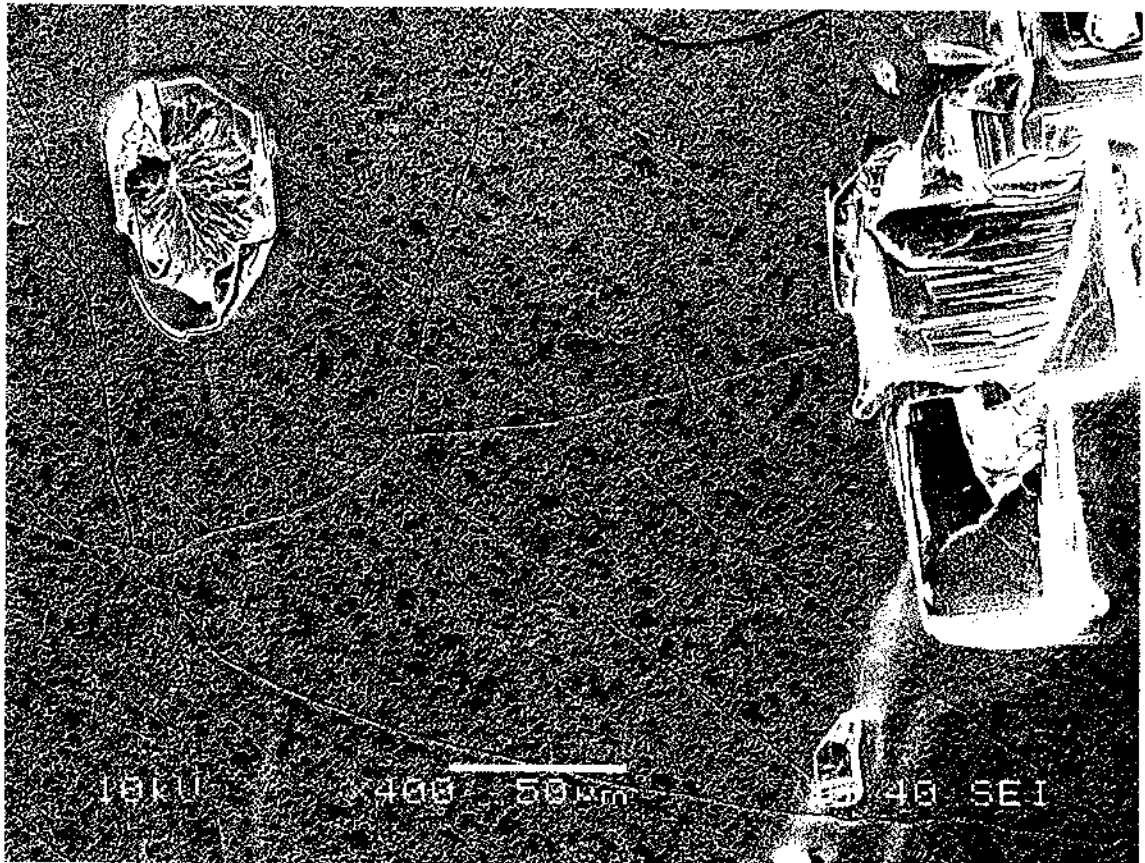

Figure 18. SEM photomicrograph showing subgrain boundaries, free dislocations and glide bands observed on cleavage chip TSDE D1.4.9, extracted from core TSDE VVS-D1-Mi4 approximately 0.9 m downhole, Northern Test Drift B (magnification: 400X).

Mean Subgrain Sizes: TSDE Test Field
Cores VVS-A-Mi4 and VVS-D1-Mi4
Extracted from the Northern Test Drift B
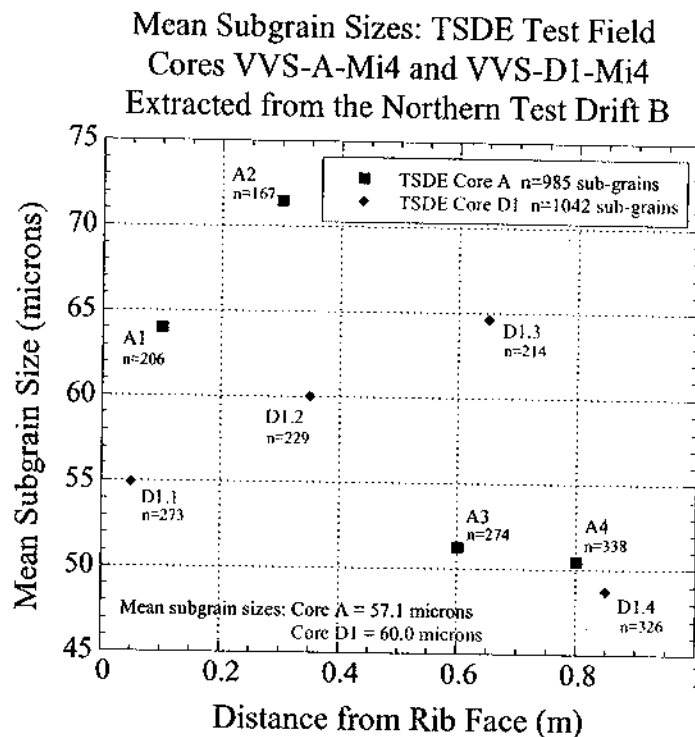
Figure 19. Plot showing the distribution of mean subgrain sizes measured from cleaved and etched chips extracted from the first meter of TSDE cores VVS-A-Mi4 and VVS-D1-Mi4, Northern Test Drift B of the TSDE Test Field, Germany.

Discussion

The microstructural analyses performed on cores reveals that the distribution of fractures is higher and that fracture apertures are wider proximal (approximately ≤ 2 m) to the rib faces. Fracture apertures existing at a depth of 2 m or greater are predominantly ≤ 100 μm wide. Therefore, a definitive damage zone exists within the first 2 m.

In WIPP Cores QGU14 and QGU36, the fracture porosity is largest proximal to the rib (≤ 2 m) and decreases consistently with increasing depth. The ALOHA II cores exhibit slightly greater porosity near the rib, but the fracture porosity becomes relatively constant at a depth > 1 m.

Investigation of fracture angles in WIPP Cores QGU36 and QGU39 reveals that the fractures closest to the rib wall trend parallel to the excavated inside face. As the fractures are mapped further out into the DRZ and into the host rock, these angles tend to increase and trend perpendicular to the core axis. Fractures that follow the stress orientation can unequivocally be ascribed to strain-induced damage, as differentiated from core-induced damage.

Substructures of both ALOHA II cores are essentially identical. The free dislocation densities of WIPP and ALOHA II cores mimic one another by displaying higher densities near the rib, which diminish at depth.

TSDE cores have the lowest measured mean dislocation densities of all the cores analyzed, which is essentially constant at 2.5×10^7 dislocations·cm^{-2}, over the entire length of the 1-m core. The relatively low dislocation density reflected here indicates that thermally-activated recovery has occurred.

The mean subgrain size observed in TSDE Cores A and D1 is approximately 60 μm (n = 027 subgrains measured). This is much smaller than previously observed subgrains from natural salts, and would indicate a steady-state stress difference of approximately 3 MPa. Glide bands are noticeable in samples containing the highest density of dislocations and measured subgrains are smallest at approximately 1 m (end of the analyses core).

References

Bryan, C.R., F.D. Hansen, D.M. Chapin, and A.C. Snider. 2001. "Characteristics of the Disturbed Rock Zone," *Proceedings: 38th U.S. Rock Mechanics Symposium; Rock Mechanics in the National Interest, Vol. 1, July 2001.* Eds. D. Elsworth, J.P. Tinucci and K.A. Heasley. Washington, DC: American Rock Mechanics Association. 511-516.

Carter, N.L., F.D. Hansen and P.E. Senseny. 1982. "Stress Magnitudes in Natural Rock Salt," *Journal of Geophysical Research.* Vol. 8, no. B11, 9289-9300.

Chapin, D.M. and F.D. Hansen. 2002. "Fracture Analyses (January 31, 2002 – July 31, 2002)," "Sandia National Laboratories Technical Baseline Reports, WBS 1.3.5.3, Compliance Monitoring WBS 1.3.5.4, Repository Investigations, Milestone RI130, July 31, 2002." Carlsbad, NM: Sandia National Laboratories. 5.1-1 to 5.1-9.

Hansen, F.D. and C.R. Bryan. 2000. "Laboratory Analysis of Samples Collected from the Disturbed Rock Zone." TP 00-04, Rev. 0. Carlsbad, NM: Sandia National Laboratories.

Holcomb, D.J. and R. Hardy. 2001. "Assessing the Disturbed Rock Zone (DRZ) at the Waste Isolation Pilot Plant in Salt Using Ultrasonic Waves Characteristics of the Disturbed Rock Zone," *Proceedings: 38th U.S. Rock Mechanics Symposium; Rock Mechanics in the National Interest, Vol. 1, July 2001.* Eds. D. Elsworth, J.P. Tinucci and K.A. Heasley. Washington, DC: American Rock Mechanics Association. 489-496.

Knowles, M.K. 1999. "Disturbed Rock Zone Characterization Program." TP 99-04, Rev. 0. Carlsbad, NM: Sandia National Laboratories.

Powers, D., C.R. Bryan and D.M. Chapin. 2001. "Laboratory Studies of Salt Cores from the WIPP Disturbed Rock Zone, (January 31, 2001 – July 31, 2001)," "Sandia National Laboratories Technical Baseline Reports, WBS 1.3.5.4, Repository Investigations, Milestone R1020, July 31, 2001." Carlsbad, NM: Sandia National Laboratories. 7-1 to 7-7.

Wieczorek, K. and U. Zimmer. 1999. "Hydraulic Behavior of the Excavation Disturbed Zone Around Openings in Rock Salt," *Proceedings: Seventh International Conference on Radioactive Waste Management and Environmental Remediation; ICEM, September 26–30, 1999; Nagoya, Japan.* New York, NY: American Society of Mechanical Engineers (available on CD-ROM only).

Sandia National Laboratories

Operated for the U.S. Department of Energy by
Sandia Corporation

Carlsbad Programs Group
4100 National Parks Highway
Carlsbad, NM 88220

date: August 29, 2002

to: Paul E. Shoemaker, MS-1395 (6820)

from: F.D. Hansen, MS-1395 (6822)
T.W. Thompson, Golder Associates

subject: Effective Permeability of the Redesigned Panel Closure System[1]

Introduction

This memorandum estimates permeabilities for the redesigned panel closure system described in the *Design Report for a Revised Panel Closure System at the Waste Isolation Pilot Plant* (Design Report) (Saeb and Case, 2002). This redesigned panel closure system consists of a mortared, solid concrete block wall placed in the panel entries over a length of 30 ft, and run-of-mine salt backfill placed on the outer side of this wall for a length of 100 ft. This backfill is not placed to any particular specifications, but it will be placed up to the back in the entry, and up to the ribs. The design report estimates the mortared block wall would exhibit a permeability of the order of 10^{-15} m^2 as emplaced. This wall is designed to continue to function throughout the operational period of 35 years, and it's permeability may be expected to remain relatively constant over this period. Beyond the 35 years the concrete wall may be expected to undergo progressive material failure and the permeability will gradually increase as the concrete block wall fractures and fails. However, the permeability of the salt backfill will reduce over time from the estimated as-emplaced value of 10^{-11} m^2 (Saeb and Case, 2002) as the loose salt consolidates. In the absence of pore pressure development, which could slow or impede consolidation, the mine-run salt may be expected to compress to very low permeability in less than 100 years. As discussed later it is not anticipated that significant pore pressures will be generated in the backfill until permeabilities of less than 10^{-15} m^2 are achieved.

The intent of this memorandum is to establish the order of magnitude of permeability of this redesigned closure as a function of time. Specifically, it demonstrates that in a fairly short time, of the order of 100 years or less, the closure system will achieve a permeability of lower than 10^{-15} m^2, and that the closure system permeability will be in the range of 10^{-15} to 10^{-19} m^2 beyond that time. The redesigned closure therefore will have a permeability in the range examined in the accompanying impact analysis (Hansen, 2002), so that the conclusions in that analysis regarding system performance can be applied to the redesigned closure. It should be noted, however, that while this memorandum demonstrates an expected range for the panel closure permeability, it is not intended to be used to define a permeability parameter for use in future Performance Assessment (PA) calculations.

---

[1] This work is covered by WBS #1.3.5.4.4.1

Panel closure design

As noted in the introduction, and described in detail in the design report (Saeb and Case, 2002), the closure comprises a mortared, solid concrete block wall 30 ft. long, and run-of-mine salt backfill 100 ft long placed to leave no gaps against the roof and ribs (Figure 1).

The resistance to fluid flow of this closure system will be a composite of the resistance to flow of the different elements, including the wall, the crushed salt and the surrounding disturbed rock zone (DRZ). Each of these components will vary in its flow resistance over time, and each will dominate over a particular time period. Since the intent of this memorandum is to review the flow resistance of the closure itself for comparison to the range examined in the impact analysis, the effect of the DRZ is not considered here, although it will be relevant to overall performance.

During the operational period the conductivity of this closure will be dominated by the mortared cement block wall, which is estimated in the design report to have a permeability of 2×10^{-15} m^2. Over time the concrete wall will gradually fracture and fail under the loads applied by the creep of the surrounding salt, and its permeability will gradually increase. However, the same creep closure which causes the concrete block wall to fail will also gradually compact the salt backfill, thus slowly decreasing its permeability and this element will come to dominate the flow performance of the closure system.

It should be noted that the relevant parameter for flow performance is in fact the flow conductance, which is a function of permeability, area, and length. However the length of the closure considered in the Compliance Certification Application (CCA) and Performance Assessment Verification Test (PAVT) calculations, and in the accompanying impact analysis, is 40 m or 131 ft, which is essentially the same as the redesigned closure, while the area is the same in the CCA, PAVT and for the redesigned closure, so the comparison may be made on the basis of permeability alone.

Salt Consolidation

Closure of the entry due to creep around the crushed salt backfill will cause the backfill to consolidate leading to loss of porosity, increase in density and reduction in permeability. The backfill void volume will be approximately 33% when placed, this being a typical value for loosely emplaced disaggregated materials and being in the range anticipated by Saeb and Case (2002). When the salt is compressed and the porosity is reduced, its permeability decreases appreciably. It has been shown that when crushed salt re-consolidates to a density approaching 95% of intact salt, its permeability is approximately 10^{-19} m^2 (Hurtado et al., 1997). It has been postulated and confirmed that consolidation of granular rock salt occurs by two primary mechanisms: grain boundary pressure solution and dislocation creep (Spiers and Brzesowsky, 1993). As crushed salt is loaded, the principal densification mechanism of fluid-phase grain boundary solution/redeposition is rampant. As consolidation proceeds, the material attains sufficient density so that its response assumes the constitutive response of intact salt, and dislocation creep becomes important. Estimates of the rate of closure and the resulting loss of permeability can be made using measured closure rates from the Panel 1 entries and laboratory data on salt consolidation.

Data on the relationship between porosity and permeability of crushed salt have been obtained in a number of laboratory experiments evaluating the behavior of backfill material in rooms and of shaft seal components. A comprehensive data set is reported by Hurtado et al., (1997) and is included as Figure A7 in Appendix SEAL of the CCA (DOE, 1996). These data are presented in Figure 2, and show that

for fractional densities above about 0.9 (equivalent to a porosity of 10%) permeabilities may be expected to be 10^{-15} m^2 or lower. If, as noted above, the run-of-mine salt is expected to have a porosity of the order of 33%, then to reach a porosity of 10% will require a volume strain of the order of 23%.

Unimpeded closure of entry drifts has been modeled and shows closure of the order of 10% in 10 years (Hansen et al., 1993). Actual measurements of roof-to-floor and rib-to-rib closure in the entries corroborate these closure rates. Figures 3 and 4 show closure data for S1600 (the Panel 1 exhaust drift) and S1950 (the Panel 1 intake drift) respectively. These data are from the E407 monitoring point which is located approximately midway between the E300 main entry and Panel 1, or in the center of the proposed panel closure locations (DOE, 2001). These data indicate that closure rates, which are summarized in the following table, are reasonably stable, and uniform, and are similar for the mid and third points of each entry. If it is assumed that the rates measured over the last ten years will continue, then the volume closure expected of the two entries is as shown in Figure 5, with closure by 25% in between 20 or 30 years.

Closure Measurement Location	Exhaust Drift (S1600) (in/day)	Air Intake Drift (S1950) (in/day)
Vertical (Center)	0.00203	0.00364
Vertical (S. third point)	0.00185	0.00300
Vertical (N. third point)	0.00196	0.00365
Mean Vertical	0.00195	0.00333
Horizontal (Upper third point)	0.00230	0.00250
Horizontal (Center)	0.00216	0.00266
Horizontal (Lower third point)	0.00200	0.00261
Mean Horizontal	0.00215	0.00259

Closure to this extent in the presence of crushed salt may be expected to be slower for three reasons. First, it is likely that a long-term slow down of closure rates may be expected, although closure by 25% in say twice the calculated time, or 40 – 60 years, is not unreasonable. Second, as the backfill consolidates it may be expected that it will stiffen and apply some back stress that will slow the closure. Case (1994) used data from Holcomb and Hannum (1982) to estimate consolidation pressure-strain curves for loosely placed backfill (Figure 6), indicating that at strains of the order of 25% imposed under rapid loading quasi-static conditions back stress of the order of 2500 psi may be expected. However creep tests carried out on similar materials by Holcomb and Hannum show that under constant stress of this magnitude the crushed salt will consolidate over time (Figure 7). This creep will result in relaxation of any potential stress build up over the tens of years being considered here, so the potential for large back stresses being induced is small. Note that this behavior is confirmed by numerical calculations of the closure of backfilled rooms (Figure 8) (Callahan and DeVries, 1991) which show closure to very low porosities in a matter of a few tens of years, and by calculations of the consolidation of dynamically emplaced crushed salt in the shaft at a depth of 600m (Figure 9).

Third, back pressure could also be applied as a result of pore pressure build-up due to gas generation in the waste. Any microbial gas generation will occur fairly rapidly, at least within the time frame discussed here, and this gas may be expected to flow through the concrete wall and into the salt backfill. However through the early parts of its consolidation, where the permeability was greater than or equal to 10^{-15} m^2, any gas generated will flow out of the backfill into any remaining void space adjacent to the

closure. As the permeability reduces still further the crushed salt may resist further consolidation, but the permeability will still be in the range estimated here.

Conclusion

When the redesigned closure is emplaced the flow resistance will be controlled by the mortared concrete block wall, and is expected to be of the order of 10^{-15} m^2. This permeability will be maintained at least through the operational period of 35 years. After this time the permeability of this element may be expected to increase somewhat as the wall degrades on an unknown time frame under creep load. At the same time the run-of-mine salt backfill will be consolidating under the creep closure of the salt surrounding the entry. Extrapolation of existing closure data suggest volume closure of the order of 25% would occur in as little as 20 to 40 years; however it is likely that this will take longer as creep closure rates will probably reduce somewhat over time. Back stress due to the consolidation is expected to be minimal over the time scales of interest (tens of years) since any tendency for stress build up will be relaxed by creep consolidation of the backfill. Once a fractional density of about 0.9 (representing a porosity of about 10%, or about 25% closure from an original porosity of 35%) is reached permeabilities of the order of 10^{-15} m^2 may be expected, and it is reasonable to expect these conditions to be reached in a maximum of 100 years. Beyond that time, permeability may be expected to decrease further with additional consolidation and values of the order of 10^{-19} m^2 may be achieved. If gas generation occurs and the gas penetrates the backfill, then as the permeability decreases, pore pressures may build up leading to a slowing or stopping of consolidation. However this will not occur until the backfill permeability reaches at least 10^{-15} m^2: at higher permeabilities the pore pressures will be relieved by flow of gas. The permeability of the closures will therefore be expected to fall in the range covered in the accompanying impact assessment, i.e. 10^{-19} to 10^{-15} m^2.

References

Callahan, G. D. and K. L. DeVries. 1991. Analyses of Backfilled Transuranic Wastes Disposal Rooms. SAND91-7052. Sandia National Laboratories, Albuquerque, NM.

Case, J.B., 1994, "Backfill Evaluation Analysis Report," Westinghouse Waste Isolation Division, Carlsbad, NM, 1994.

Hansen, C., "Analysis Report for the Panel Closure Impact Assessment," Sandia National Laboratories, Carlsbad NM, August, 2002.

Hansen, F.D., M.S. Lin, L.L. VanSambeck, 1993. "Concept for Operational Period Seal Design at the Waste Isolation Pilot Plant," SAND93-0729, July 1993.

Holcomb, D.J. and D.W. Hannum, 1982, "Consolidation of Crushed Salt Backfill Under Conditions Appropriate to WIPP," SAND82-0630, November 1982.

Hurtado, L.D., M.K. Knowles, V.A. Kelley, T.L. Jones, J.B. Ognitz, T.W. Pfeifle, 1997. "WIPP Shaft Seal System Parameters Recommended to Support Compliance Calculations," SAND97-1287, December 1997.

Saeb, S and J. Case, 2002, "Design Report For A Revised Panel Closure System At The Waste Isolation Pilot Plant," Report to Westinghouse TRU Solutions, LLC., Rocksol Inc., Boulder CO.

Spiers, C.J., and R.H. Brzesowsky. 1993. "Densification Behavior of Wet Granular Salt: Theory Versus Experiment," *Seventh Symposium on Salt,* Kyoto, Japan, April 6-9, 1992. Eds. H. Kakihana, H.R. Hardy, Jr., T. Hoshi, and K. Toyokura. Amsterdam; New York, New York: Elsevier Science Publishers B.V. Vol. I, 83-92.

U.S. Department of Energy, 1996, "Title 40 CFR 191 Compliance Certification Application for the WIPP: Appendix SEAL," Carlsbad NM, 1996.

U.S. Department of Energy, 2001, "Geotechnical Analysis Report for July 1999-June 2000," DOE/WIPP 01-3177, Waste Isolation Pilot Plant, Carlsbad, New Mexico.
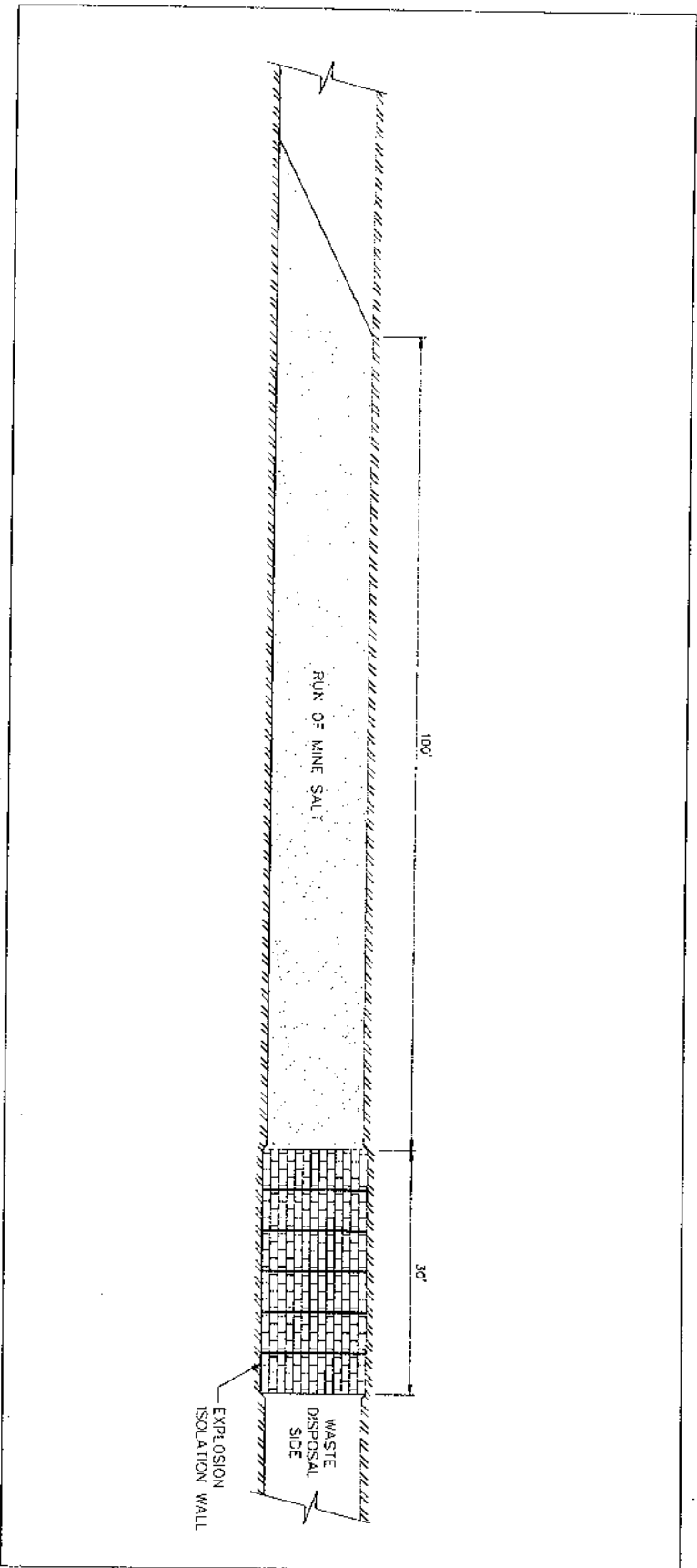
Figure 1. Explosion Isolation Wall in Combination with the Run-of-Mine Salt Backfill (Saeb and Case, 2002)
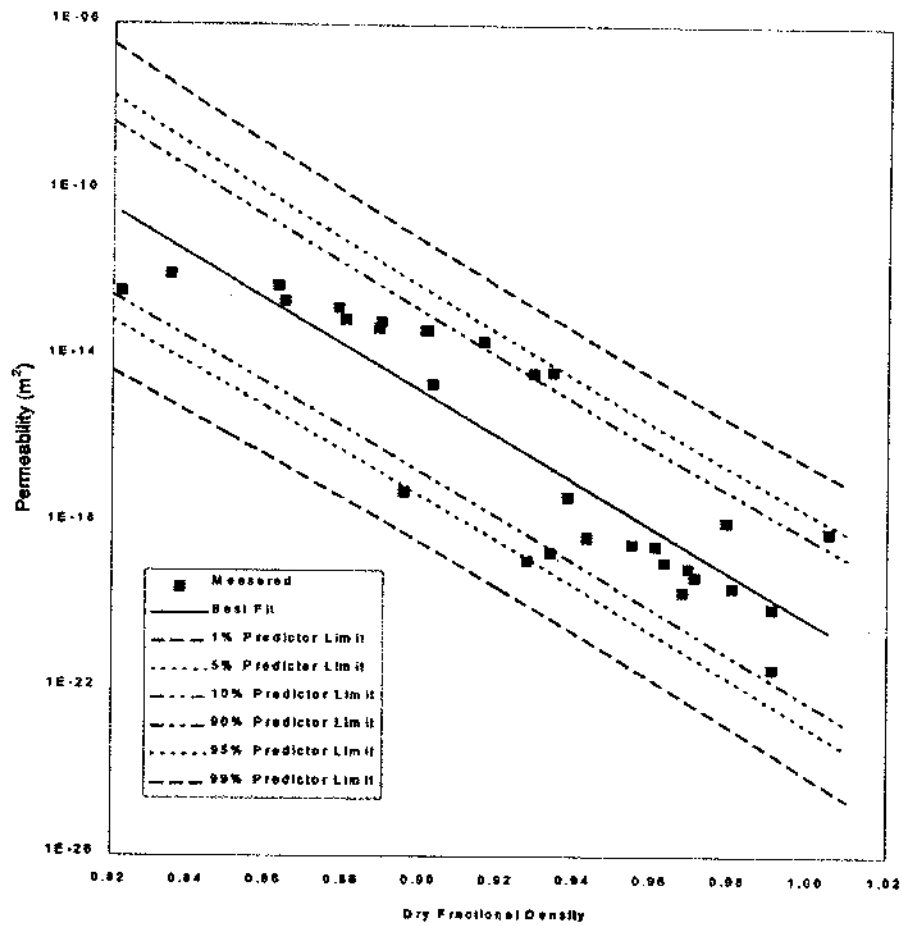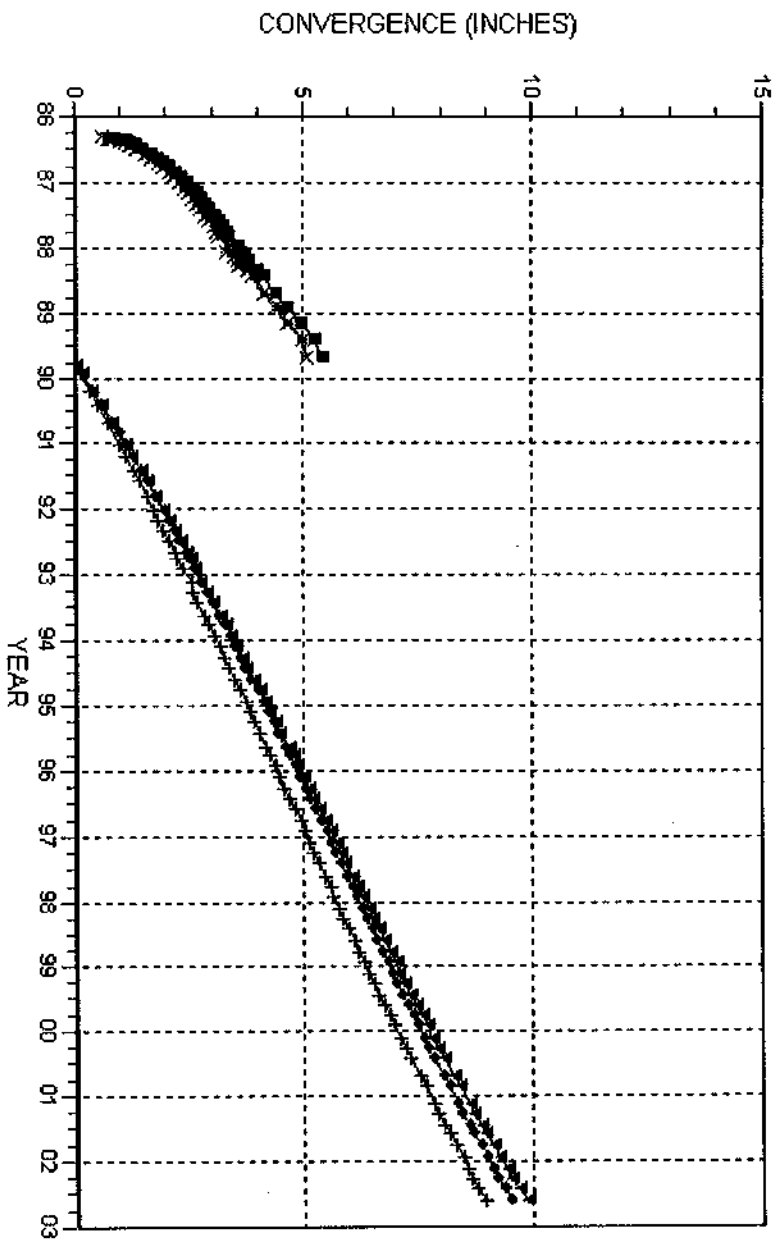
Figure 2. Permeability of Consolidated Crushed Salt as a Function of Fractional Density (DOE, 1996)

Figure 3: Closure Data for the Exhaust Drift (S1600) (DOE, 2001)
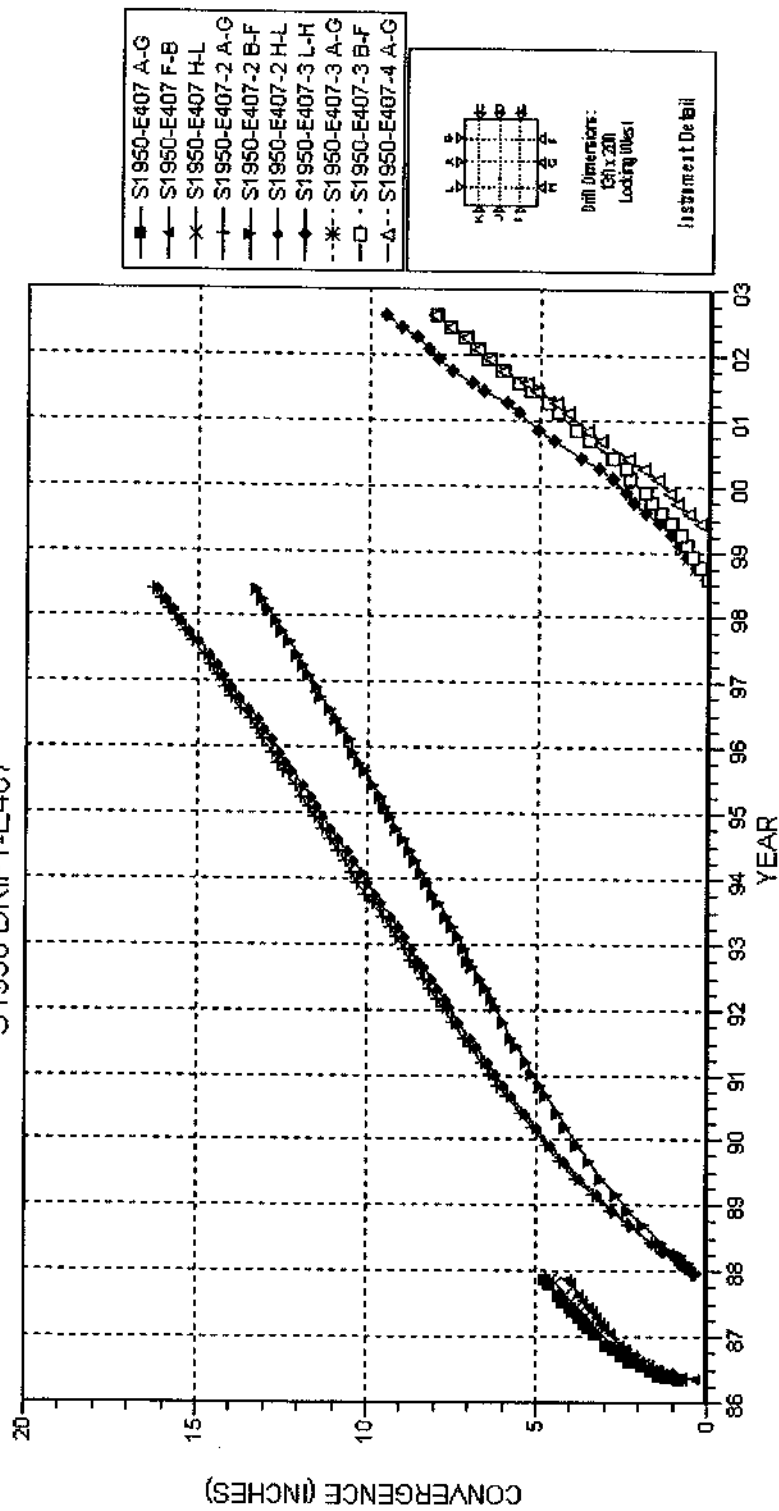
CONVERGENCE POINTS
S1600 DRIFT-E407

CONVERGENCE (INCHES)

YEAR

NOTES:
1. Excavation date: April 1986.

- S1600-E407 A-G
- S1600-E407 F-B
- S1600-E407 H-L
- S1600-E407-2 B-F
- S1600-E407-2 A-G
- S1600-E407-2 L-H

Drift Dimensions:
120h x 14ft
Looking ODes I

Instrument Detail

Figure 4: Closure Data for the Air Intake Drift (S1950) (DOE, 2001)

NOTES:
1. Excavation date: May 1986.

5.3-9
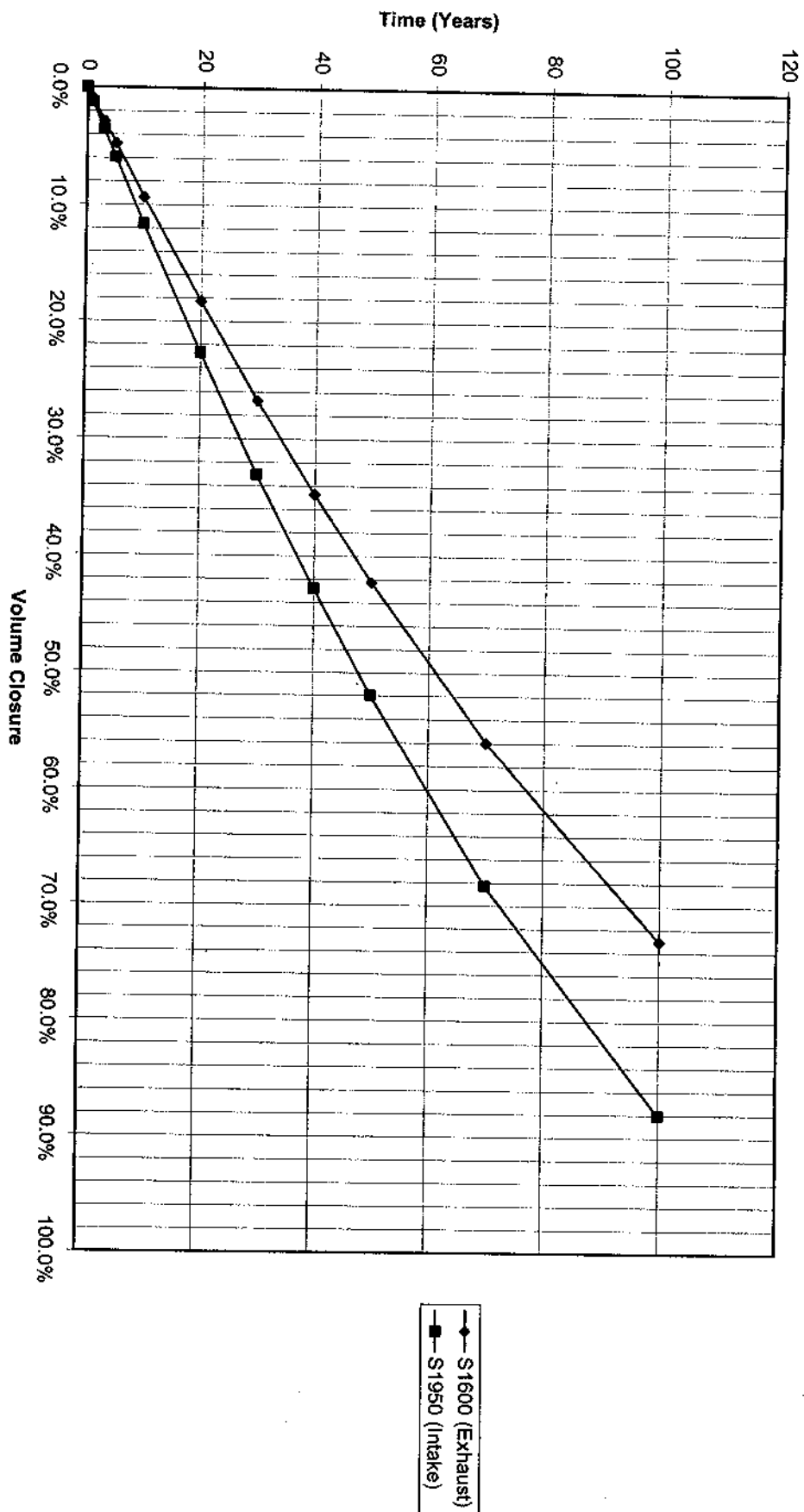
Drift Closure

Figure 5. Calculated Drift Closure Assuming Constant Closure Rates and no Backstress

Legend:
- S1600 (Exhaust)
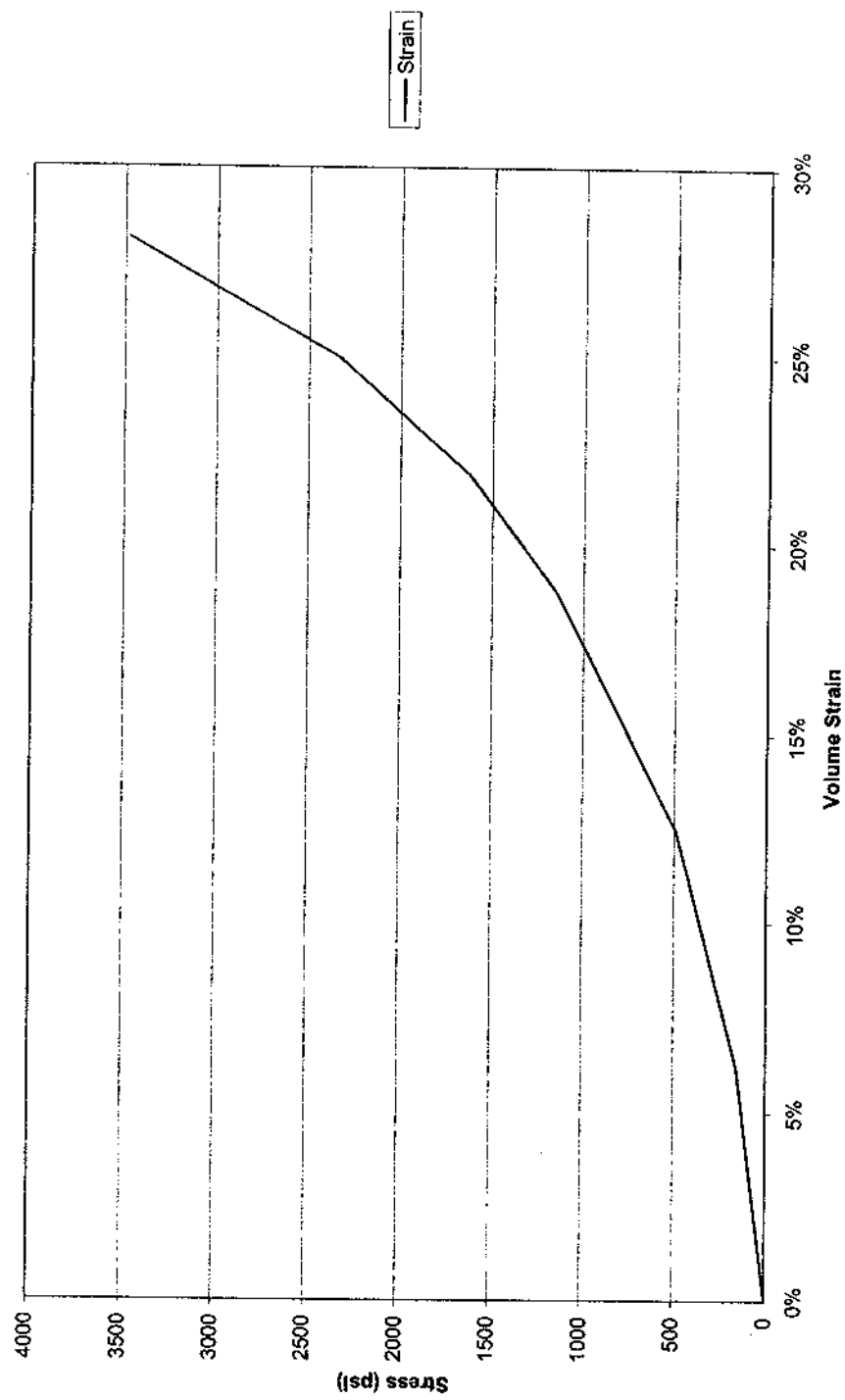- S1950 (Intake)

Quasi-Static Consolidation Data

Figure 6: Quasi-Static Consolidation Data for Dry Crushed Salt (after Holcomb and Hannum, 1982 and Case, 1994)
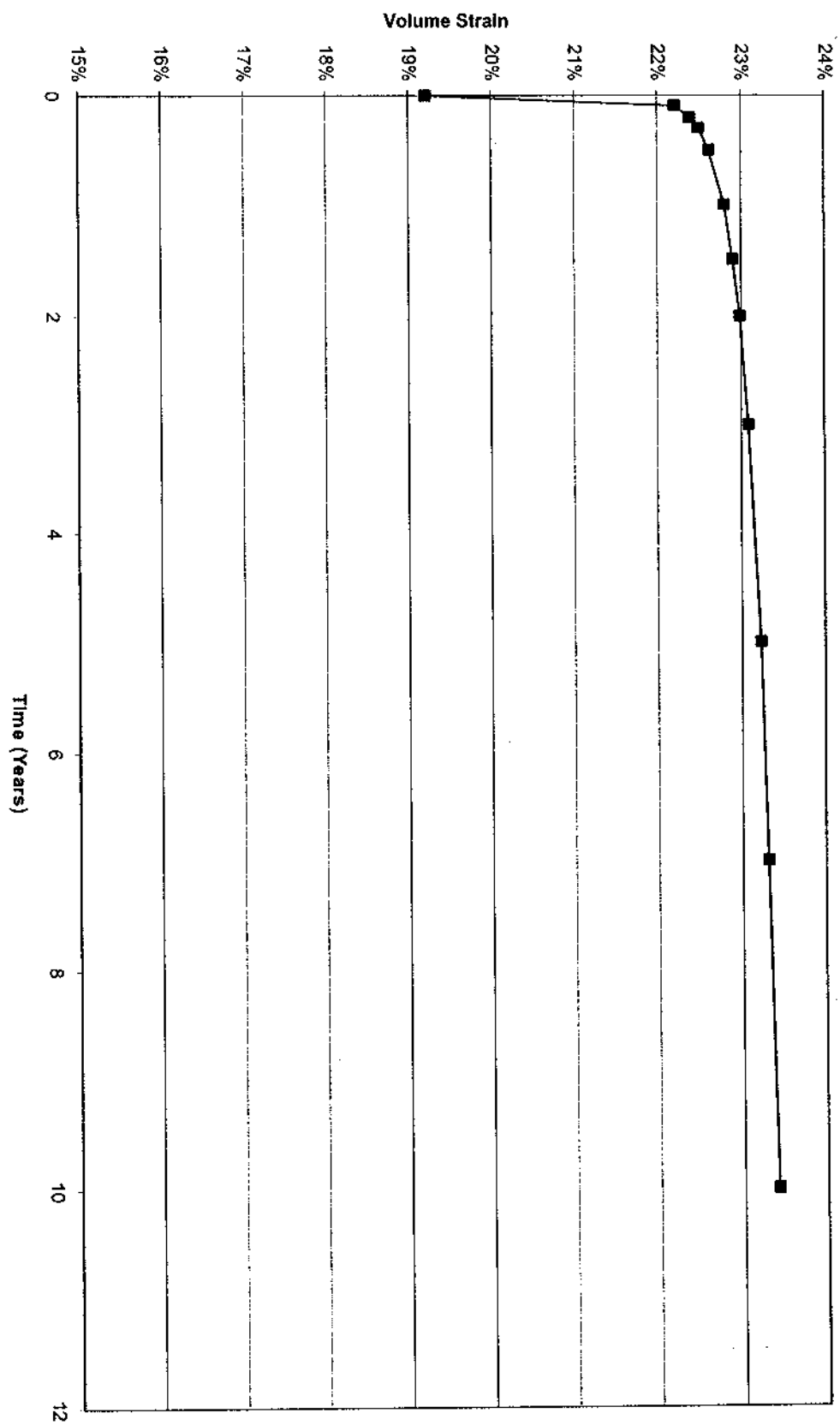
5.3-11

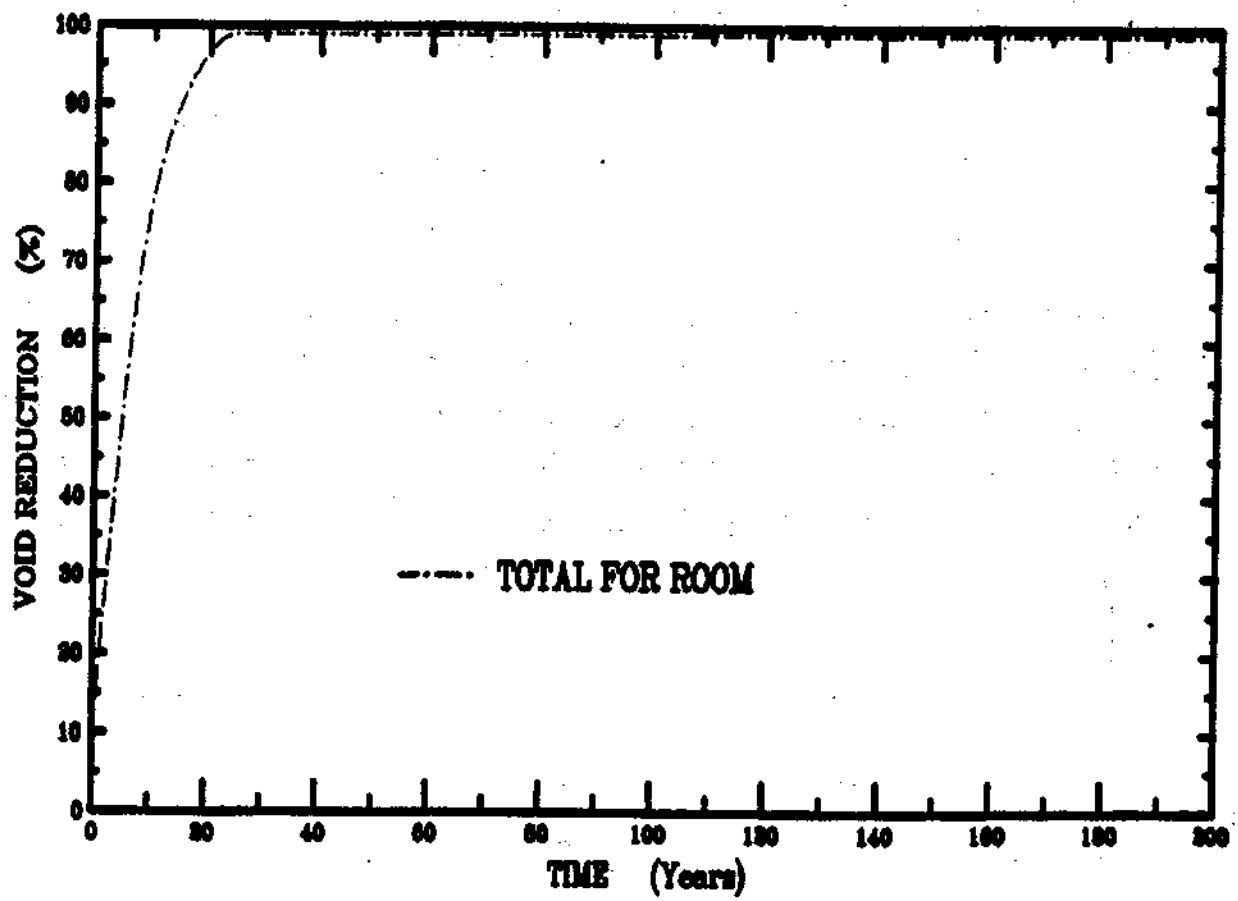Figure 7: Creep Consolidation Data for Dry Crushed Salt (after Holcomb and Hannum, 1982)

Figure 8. Void Reduction in a Disposal Room filled with Crushed Salt as a Function of Time (Callahan and DeVries, 1991).
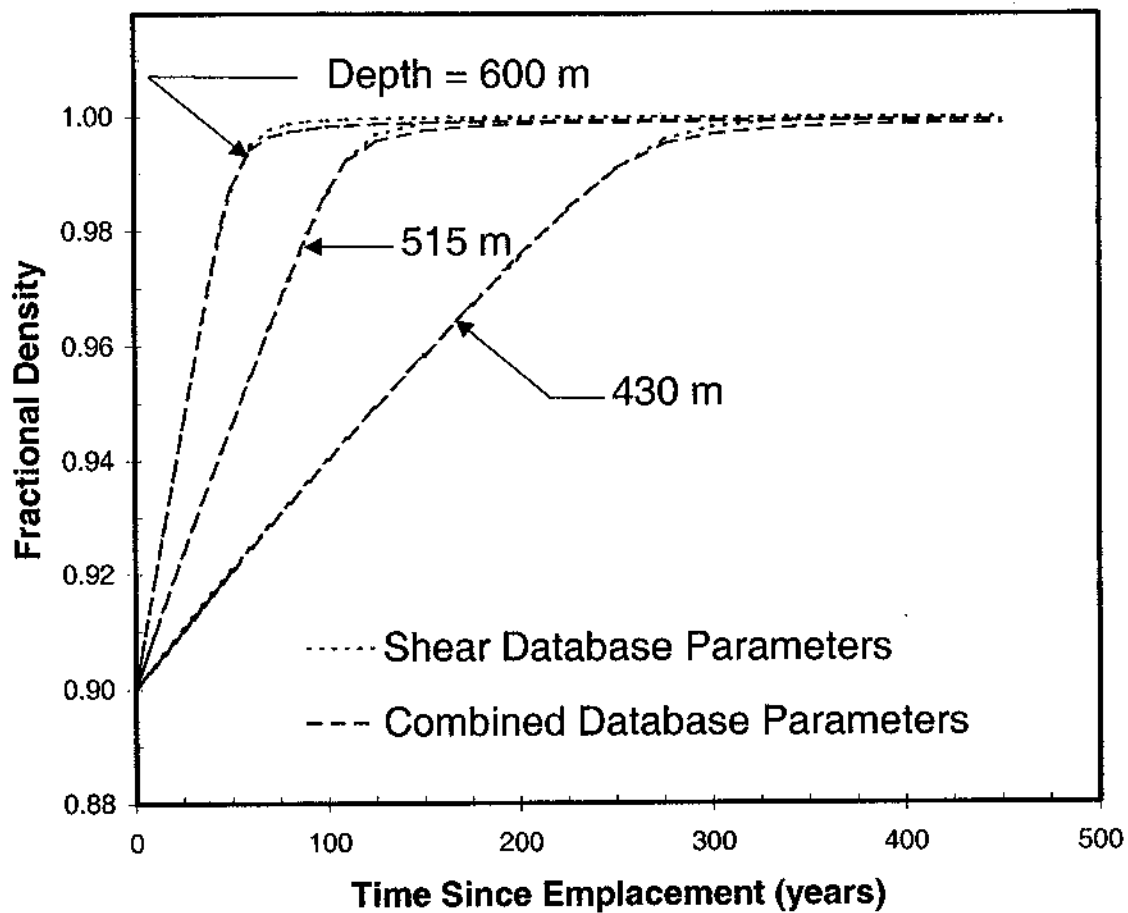
Figure 9. Calculated Fractional Density Versus Time for Crushed Salt Compacted in the Shaft.